An Inverse Model for Estimating the Optical Absorption and Backscattering Coefficients of Seawater From Remote-Sensing Reflectance Over a Broad Range of Oceanic and Coastal Marine Environments

Hubert Loisel, Dariusz Stramski, David Dessailly, Cédric Jamet, Linhai Li, Rick Reynolds

AGU PUBLICATIONS

JGR

Journal of Geophysical Research: Oceans

RESEARCH ARTICLE

10.1002/2017JC013632

An Inverse Model for Estimating the Optical Absorption and Backscattering Coefficients of Seawater From Remote-Sensing Reflectance Over a Broad Range of Oceanic and Coastal Marine Environments

Hubert Loisel[1,2], Dariusz Stramski[3], David Dessailly[1], Cédric Jamet[1,2], Linhai Li[3], and Rick A. Reynolds[3]

[1]Laboratoire d'Océanologie et de Géosciences, Université du Littoral Côte d'Opale, Université Lille, CNRS, UMR 8187, LOG, Wimereux, France, [2]Hanoi International Laboratory of Oceanography, University of Science and Technology of Hanoi, Vietnam Academy of Science and Technology, Cau Giay, Vietnam, [3]Marine Physical Laboratory, Scripps Institution of Oceanography, University of California San Diego, La Jolla, CA, USA

Key Points:
- An improved inverse reflectance model for estimating ocean inherent optical properties (IOPs) with no spectral assumptions was developed
- Model evaluation with a synthetic data set indicates that algorithmic formulations are adequate, which results in good IOP retrievals
- Satisfactory model performance is validated with extensive data sets of in situ measurements and a satellite-in situ match-up data set

Supporting Information:
- Supporting Information S1

Correspondence to:
H. Loisel,
hubert.loisel@univ-littoral.fr

Citation:
Loisel, H., Stramski, D., Dessailly, D., Jamet, C., Li, L., & Reynolds, R. A. (2018). An inverse model for estimating the optical absorption and backscattering coefficients of seawater from remote-sensing reflectance over a broad range of oceanic and coastal marine environments. *Journal of Geophysical Research: Oceans*, *123*, 2141–2171. https://doi.org/10.1002/2017JC013632

Received 13 NOV 2017
Accepted 5 JAN 2018
Accepted article online 20 FEB 2018
Published online 25 MAR 2018

Abstract We present an inverse model (referred to as LS2) for estimating the inherent optical properties (IOPs) of seawater, specifically the spectral absorption, $a(\lambda)$, and backscattering, $b_b(\lambda)$, coefficients within the ocean surface layer, from measurements of ocean remote-sensing reflectance, $R_{rs}(\lambda)$. The nonwater absorption, $a_{nw}(\lambda)$, and particulate backscattering, $b_{bp}(\lambda)$, coefficients can be derived after subtracting pure seawater contributions. The LS2 requires no spectral assumptions about IOPs and provides solutions at arbitrary light wavelengths in the visible spectrum independently of one another. As the LS2 can operate with the inputs of $R_{rs}(\lambda)$ and solar zenith angle it is applicable to satellite ocean color remote sensing. The model can also operate with additional input of the diffuse attenuation coefficient of downward irradiance, which provides somewhat improved model performance for applications using in situ radiometric measurements as inputs. The evaluation of LS2 with a synthetic data set that is free of measurement errors indicates good performance for IOPs in the visible spectrum, except for $a_{nw}(\lambda)$ in the long-wavelength portion of the spectrum where $a_{nw}(\lambda)$ contributes only a few percent to $a(\lambda)$ under typical open ocean conditions. The good performance is characterized by a median absolute percent difference between the model-derived and true values of IOPs, which is generally $<20\%$, and the median ratio of model-derived to true values $<10\%$. The satisfactory model performance is also demonstrated through validation analysis based on extensive data sets comprising coincident in situ measurements of $R_{rs}(\lambda)$ and IOPs as well as a match-up data set comprising satellite-derived $R_{rs}(\lambda)$ and in situ IOP measurements.

1. Introduction

The last two decades have been characterized by an increased interest in inverse methods dedicated to the estimation of inherent optical properties (IOPs) of natural surface waters from ocean color remote-sensing observations (e.g., IOCCG, 2006; Werdell et al., 2013). The IOPs are determined by constituents of seawater, including water molecules, planktonic organisms, nonalgal particulate matter (organic detritus and mineral particles), gas bubbles, and colored dissolved organic matter (CDOM, also known as yellow substance). Whereas the pure seawater IOPs are quite stable, depending somewhat on water temperature and salinity, large variability in bulk IOPs observable in the ocean is tightly linked to variations in the concentration of these different constituents, the size distribution and chemical composition of particulate matter, and the chemical composition of dissolved organic matter. These linkages make the IOPs an attractive carrier of information about various biogeochemically important constituents of seawater, for example, the particulate and dissolved stocks of carbon and phytoplankton community structure. The ability to retrieve IOPs within the surface ocean from space observations of ocean color is particularly beneficial to improving the investigations of biogeochemical status of the surface oceanic layer at large basin and global scales over long periods of time beyond the application of the standard satellite data product of chlorophyll-*a* concentration, *Chl* (in units of mg m^{-3}). For this reason, the IOPs are now included in the suite of Essential Climate Variables within the framework of the Climate Change Initiative international program (Lavender et al., 2015).

In general, two IOPs are commonly estimated from the ocean spectral remote-sensing reflectance, $R_{rs}(\lambda)$ (in units of sr^{-1}), which is derivable from satellite ocean color measurements; the spectral backscattering coefficient, $b_b(\lambda)$, and the spectral absorption coefficient, $a(\lambda)$ (both in units of m^{-1}), of seawater (λ represents the wavelength of light in vacuum in units of nm). Many extant models or algorithms for IOP retrieval yield the component absorption coefficients associated with phytoplankton, $a_{ph}(\lambda)$, and colored detrital matter (CDM) that includes combined contributions of nonalgal particles (NAP) and CDOM, $a_{cdm}(\lambda)=a_{NAP}(\lambda)+a_{CDOM}(\lambda)$, as well as the particulate backscattering coefficient, $b_{bp}(\lambda)$, which is the difference between $b_b(\lambda)$ and the pure seawater backscattering coefficient, $b_{bw}(\lambda)$. Note that the sum of $a_{ph}(\lambda)$, $a_{NAP}(\lambda)$, and $a_{CDOM}(\lambda)$ can be referred to as the nonwater absorption coefficient, $a_{nw}(\lambda)$, which can also be derived as a difference between $a(\lambda)$ and pure seawater absorption coefficient, $a_w(\lambda)$. Satellite-derived IOP data products have been used in many studies addressing various characteristics of seawater constituents of biogeochemical significance (e.g., Balch et al., 2005; Behrenfeld et al., 2013; Kostadinov et al., 2009, 2010; Loisel et al., 2001a, 2002; Mannino et al., 2008; Siegel et al., 2002; Stramski et al., 1999; Vantrepotte et al., 2011), oceanic primary production (e.g., Behrenfeld et al., 2005; Lee et al., 2011), and characterization of water masses and other physical processes (e.g., Arnone et al., 2004; Traykovski & Sosik, 2003; Yang et al., 2015).

Different approaches have been proposed to derive IOPs within the surface ocean layer from satellite ocean color data (e.g., IOCCG, 2006; Werdell et al., 2013). Empirical models are among the most straightforward approaches as they are simply based on statistical relationships between IOPs and $R_{rs}(\lambda)$, or an equivalent quantity characterizing ocean color. Example empirical relationships for estimating total and component absorption coefficients from spectral band ratios of remote-sensing reflectance are described in Lee et al. (1998), Stramska et al. (2003), and Pan et al. (2008). Empirical algorithms for estimating the backscattering coefficient from remote-sensing reflectance have been also proposed (e.g., Stramski et al., 1999, 2008). Neural network approaches also fall into the category of empirical approaches (e.g., Chen et al., 2014; Doerffer & Schiller, 2007). The empirical algorithms can perform reasonably well, especially when applied on a regional/seasonal basis consistent with the data set used in the algorithm development. In general, however, the formulation and performance of empirical algorithms can depend significantly on several factors such as the size and accuracy of field measurements required for the algorithm development, seasonal and spatial coverage of field measurements used in the algorithm development, effects of variables unaccounted for in the algorithm, and environmental changes that require modifications to statistical relationships. Therefore, recent research efforts to derive IOPs in the context of ocean color remote sensing have focused on the use of semianalytical (or semiempirical) inverse reflectance models.

Semianalytical models are essentially based on the analytical link between $R_{rs}(\lambda)$ and IOPs established from radiative transfer theory (Gordon et al., 1975, 1988; Morel & Prieur, 1977). Most extant semianalytical models aim at simultaneously estimating the backscattering and absorption components of total IOPs (such as b_{bp}, a_{ph}, a_{cdm}) using reflectance data as input to the inversion algorithms (e.g., Brando et al., 2012; Bukata et al., 1995; Devred et al., 2006; Garver & Siegel, 1997; Hoge & Lyon, 1996; Maritorena et al., 2002; Roesler & Perry, 1995; Wang et al., 2005). In this type of model, the linear or nonlinear optimization schemes are usually applied to an approximate functional relationship that links ocean reflectance and component IOPs. In essence, the simultaneous solutions for the component IOPs are searched by minimizing differences between the measured and modeled reflectance values. There also exist inverse models in which the total IOPs of seawater are derived or the derivation of total IOPs is followed by the estimation of component IOPs (Lee et al., 2002; Loisel & Stramski, 2000; Pinkerton et al., 2006; Smyth et al., 2006). This type of inverse model is usually based on algebraic algorithms operating in a stepwise fashion, possibly also involving some iterative schemes. An important characteristic of algorithms yielding total IOPs is that they make it possible to apply the stand-alone independently developed models for partitioning the total IOPs into component IOPs, which do not require reflectance data as input to the partitioning algorithms, for example, the absorption partitioning models (e.g., Ciotti & Bricaud, 2006; Zhang et al., 2015; Zheng et al., 2015; Zheng & Stramski, 2013).

An important limitation affecting the performance of most extant semianalytical models is a requirement for a priori assumptions about the spectral shape of model output of component absorption and backscattering coefficients. Typically, such assumptions do not adequately represent the whole range of natural variability in these properties, resulting in potentially large uncertainties in model-derived IOPs, especially in

applications for arbitrary time and location within the global ocean. Moreover, the assumed spectral shapes are often constrained to the visible part of the spectrum and their extension to other spectral bands in the ultraviolet (UV) or near-infrared (NIR) may not be warranted. To better account for naturally occurring variability in IOPs, the implementation of variable model parameters encompassing variations in spectral shape of component IOPs has been explored (Brando et al., 2012; Wang et al., 2005) or a priori assumptions of IOP spectral shapes have been completely relaxed (Loisel & Stramski, 2000).

The model of Loisel and Stramski (2000), hereafter referred to as LS1, is of particular interest as it requires no assumptions regarding the spectral behavior of derived IOPs. Our primary objective in this study is to develop modifications and improvements to LS1, which lead to better estimation of $a(\lambda)$ and $b_b(\lambda)$ from ocean color remote sensing within a broad range of open ocean and marine coastal environments. First, we provide an overview of the original version of the LS1 model and the reasons for its modifications and improvements. Next, we describe the development and formulation of a new model, i.e., a modified version of LS1 that is hereafter referred to as LS2. Radiative transfer simulations supporting this task are included in this description. The next section is devoted to the evaluation of the LS2 model and its validation in the context of both in situ and remote-sensing applications. A synthetic data set is first used for model evaluation. Because this data set is not subject to measurement errors, it allows evaluating the model and providing uncertainties for each derived parameter, which depend solely on the algorithmic formulation of the model. Field data sets of coincident in situ $R_{rs}(\lambda)$ and IOP measurements are used to validate the model for a broad range of environments from ultraoligotrophic open ocean waters to very turbid coastal waters. This validation exercise includes the effects associated with uncertainties in both the model itself and in situ measurements. Finally, the model is validated in the context of remote-sensing application. For this purpose we use a match-up data set, in which the model input of remote-sensing reflectance, $R_{rs}(\lambda)$, derived from satellite observations is accompanied by coincident in situ IOP measurements. This analysis allows assessment of the performance of the model when subject to various sources of uncertainty including uncertainties in satellite-derived $R_{rs}(\lambda)$.

2. Overview of the LS1 Model and Required Improvements

The LS1 model was developed on the basis of radiative transfer simulations to enable the estimation of three IOPs, the total spectral absorption, $a(\lambda)$, spectral scattering, $b(\lambda)$, and spectral backscattering, $b_b(\lambda)$, coefficients within the surface ocean, from the irradiance reflectance just below the sea surface, $R(z=0^-, \lambda)$ (dimensionless), and the average attenuation coefficient for downwelling irradiance, $<K_d(\lambda)>_1$ (in units of m^{-1}), between the surface and the first attenuation depth, z_1 ($z=0^-$ represents depth just below the surface). The simulations are described in detail in Morel and Loisel (1998) and Loisel and Stramski (2000). The input variables $R(0^-, \lambda)$ and $<K_d(\lambda)>_1$ to the LS1 model belong to the class of the apparent optical properties (AOPs) of the ocean (e.g., Mobley, 1994). The depth z_1, at which the downwelling irradiance is reduced by 37% of its surface value, is of particular importance in ocean color remote sensing because 90% of the water-leaving upwelling photons that can be detected by a satellite sensor originate within the oceanic layer between the surface and z_1 (Gordon & McCluney, 1975).

The key feature of LS1 is that it solves for IOPs at any arbitrary light wavelength, λ, independently of other wavelengths without any assumptions about the spectral shape of the derived IOPs. The LS1 model is based on the following set of basic equations linking $a(\lambda)$, $b_b(\lambda)$, $<K_d(\lambda)>_1$, and $R(0^-, \lambda)$, which are applicable to any arbitrary light wavelength (in the equations we omit λ for the sake of brevity):

$$a=\mu_w <K_d>_1 \frac{1}{\left[1+h(\mu_w)\frac{R(0^-)}{1-R(0^-)}\right]^{0.5}} \tag{1}$$

$$b_b= <K_d>_1 10^{\alpha} [R(0^-)]^{\delta} \tag{2}$$

The h, α, and δ functions are given by:

$$h=2.54-6.54\mu_w+19.89\,\mu_w^2 \tag{3}$$

$$\alpha=\left(-0.83+5.34\eta-12.26\eta^2\right)+\mu_w\left(1.013-4.124\eta+8.088\eta^2\right) \tag{4}$$

$$\delta = \left(0.871 + 0.4\eta - 1.83\eta^2\right) \quad (5)$$

where $\eta(\lambda)$ (dimensionless) is the ratio of the water molecular scattering coefficient, $b_w(\lambda)$, to the total scattering coefficient, $b(\lambda)$ (both coefficients in units of m^{-1}), and μ_w (dimensionless) is the cosine of the angle of refraction of the solar beam just beneath the sea surface. The parameter μ_w is calculated as $\mu_w = \cos\left[\sin^{-1}\left(\sin\theta_s / n_w\right)\right]$ where n_w is the refractive index of water and θ_s is the solar zenith angle. A typical assumption is $n_w = 1.34$. The $\eta(\lambda)$ parameter is obtained through the computation of $b(\lambda)$ as a function of $<K_d(\lambda)>_1$ and $R(0^-, \lambda)$ (see equations (13) and (14) in Loisel and Stramski, 2000). These basic equations of LS1 were developed under the assumption of no inelastic radiative processes in the ocean, such as Raman scattering by water molecules. Therefore, the input AOPs to these equations represent a hypothetical scenario with no inelastic processes, which may lead to significant uncertainties, especially in the green and red portions of the spectrum where Raman scattering may have an important influence on the underwater light field and AOPs (e.g., Marshall & Smith, 1990; Stavn, 1993; Sugihara et al., 1984). The LS1 model includes, however, an additional component that corrects for the presence of Raman scattering, thus improving the realism of modeled marine optical environment and the retrieval of IOPs. Another important point is that in the context of remote-sensing applications, the required input data of $R(0^-, \lambda)$ and $<K_d(\lambda)>_1$ to LS1 are not measured by ocean color sensors, but must be derived from the primary ocean color data product, such as remote-sensing reflectance, $R_{rs}(\lambda)$ (see Loisel et al., 2001b). A slightly modified version of LS1 was developed and tested as part of the International Ocean Colour Coordinating Group (IOCCG) Working Group dedicated to inverse bio-optical algorithms (IOCCG, 2006). The main improvement involved a new empirical formulation to compute $<K_d(\lambda)>_1$ at 410, 440, 510, and 550 nm from $R_{rs}(490)/R_{rs}(550)$ (Loisel & Poteau, 2006).

Although LS1 has already been used in a number of studies utilizing satellite observations of ocean color (e.g., Bricaud et al., 2012; Ciotti & Bricaud, 2006; Duforêt-Gaurier et al., 2010; Dupouy et al., 2003; Kostadinov et al., 2009, 2010; Loisel et al., 2001a, 2002; Vantrepotte et al., 2011), there are several compelling reasons to conduct new radiative transfer simulations with a purpose to modify and improve the model for such applications. First, while $R(0^-, \lambda)$ can be determined directly from in situ measurements, it is $R_{rs}(\lambda)$ and not $R(0^-, \lambda)$ which is derived as the primary ocean data product from ocean color remote-sensing observations. Therefore, in this study we use $R_{rs}(\lambda)$ instead of $R(0^-, \lambda)$ as input to the new model LS2. Second, we use a neural network approach (Jamet et al., 2012) to estimate $<K_d(\lambda)>_1$ from $R_{rs}(\lambda)$, instead of the empirical relationships used previously in the original LS1 and its version from the IOCCG project in 2006. An improvement of the neural network algorithm of Jamet et al. (2012) is also included in the LS2 model. Third, the derivation of $\eta(\lambda)$ in LS1 is directly linked to the retrieval accuracy of $b(\lambda)$ which is strongly dependent on the scattering phase function of particles (Loisel & Stramski, 2000). An accurate retrieval of $b(\lambda)$ can therefore be achieved only when the phase function for the observed water body is similar to that used for the model parameterization based on specific set of radiative transfer calculations. In the LS2 model, a new procedure is used to estimate $\eta(\lambda)$. The next motivation factor for model improvements is associated with a need for the use of realistic combinations of values for the b/a and η parameters in the radiative transfer simulations and subsequent parameterization of the model. Finally, compared with the development of LS1, the range of IOPs included in radiative transfer simulations for developing the LS2 model in this study is significantly extended, especially to extend coverage into highly turbid waters.

3. Model Development and Formulation

3.1. Radiative Transfer Simulations

Similar to the LS1 model, in this study the modifications of LS1 and the resultant LS2 model are developed on the basis of two sets of simulations of radiative transfer within the ocean. The first set of simulations (S1) is used for the development of model equations and parameterizations in the absence of Raman scattering by water molecules. The second set (S2) is used for developing a correction for the presence of Raman scattering. Fluorescence processes associated with CDOM and phytoplankton were not included in the simulations. Both sets of simulations were performed with the Hydrolight v5.0 radiative transfer code (Mobley & Sundman, 2008) for a homogeneous and infinitely deep ocean with the modeled roughness of the sea surface corresponding to wind speed of 5 m s^{-1}. All simulations were made assuming clear skies and standard atmosphere, where the normalized sky radiances were computed using the sky model "HCNRAD," and diffuse and direct sky irradiances were computed using the "RADTRANX" model, as implemented in the

Hydrolight code. The required atmospheric parameters (air mass type, pressure, visibility, ozone, precipitable water, relative humidity, 24 h wind speed) were set to their default values. In addition, for a given set of input variables, the Hydrolight runs were made for different sun zenith angles, θ_s, ranging from 0° to 70° with a step of 10°. The use of clear sky conditions has been motivated by our primary interest in the development of the model for ocean color remote-sensing applications that require clear skies.

The IOPs of seawater used as input in S1 are represented by two dimensionless quantities, the ratio of total scattering coefficient to absorption coefficient of seawater, b/a, and the ratio of molecular scattering coefficient to total scattering coefficient of seawater, η. The use of these two dimensionless quantities irrespective of light wavelength allows the model to be developed without any assumptions about the spectral shape of IOPs. The absorption coefficient is fixed at 1 m^{-1}, and the b/a ratio varies from 0.05 to 30 (0.05, 0.10, 0.15, 0.2, 0.3, 0.4, 0.5, 0.6, 0.7, 0.8, 0.9, 1.0, 1.5, 2.0, 2.5, 3.0, 3.5, 4.0, 4.5, 5.0, 5.5, 6.0, 7.0, 8.0, 9.0, 10.0, 12.0, 14.0, 16.0, 18.0, 20.0, 22.0, 24.0, 26.0, 28.0, 30.0). The variation of the total scattering phase function of seawater (in units of sr^{-1}) is driven through the η parameter that provides the respective contributions of molecular and particulate scattering to the total phase function (see equation (2) in Loisel and Stramski, 2000). We assumed the same phase functions for molecular and particulate scattering as Loisel and Stramski (2000). Specifically, the molecular phase function was calculated from an appropriate formulation for scattering by water molecules (Mobley, 1994). For particles, we used the phase function proposed in Mobley (1994), which was derived by averaging three particle phase functions measured in oceanic waters by Petzold (1972). Because the estimation of the total absorption and backscattering coefficients from this type of model has been shown to be weakly sensitive to variations in the particle phase function (Gordon, 1993; Loisel & Stramski, 2000), the use of a single particle phase function in the model development is warranted. The simulations were run with the following η values: 0.000, 0.005, 0.015, 0.020, 0.025, 0.030, 0.035, 0.040, 0.045, 0.050, 0.055, 0.060, 0.065, 0.070, 0.075, 0.080, 0.085, 0.090, 0.100, 0.150, and 0.200. We emphasize that the development of the LS2 model is based on the use of realistic combinations of b/a and η values. The criteria for the selection of the (b/a, η) data pairs used in Hydrolight simulations were based on standard bio-optical models for oceanic Case 1 waters and available in situ data sets for coastal waters. For instance, a combination of high b/a and η values is not realistic in Case 1 waters (see Figure 2 in Morel and Loisel, 1998), and thus is not included in the simulations.

Raman scattering can contribute significantly to the remote-sensing reflectance in the green and red parts of the spectrum (15% or more) in oligotrophic waters (e.g., Gordon, 1999; Stavn, 1993; Westberry et al., 2013). To account for Raman scattering in the model development, radiative transfer simulations (S2) have been performed with and without Raman scattering. In S2, the IOPs of seawater were modeled as a function of light wavelength and *Chl* by means of standard bio-optical models for oceanic Case 1 waters provided in the library of subroutines of Hydrolight. Simulations with and without Raman scattering were made within the wavelength range from 350 to 700 nm for the following *Chl* values: 0.01, 0.02, 0.03, 0.04, 0.05, 0.06, 0.07, 0.08, 0.09, 0.1, 0.2, 0.3, 0.4, 0.5, 0.6, 0.7, 0.8, 0.9, 1.0, 2.0, 3.0, 4.0, and 5.0 mg m^{-3}. Because the shortest wavelength in the simulations is 350 nm, the effect of Raman scattering is examined in the visible part of the spectrum for wavelengths longer than 400 nm.

3.2. Model Parameterization

The LS2 model is formulated to enable the estimation of two IOPs of seawater within the surface ocean layer, the spectral backscattering, $b_b(\lambda)$, and spectral absorption, $a(\lambda)$, coefficients, from input data of $R_{rs}(\lambda)$ and $<K_d(\lambda)>_1$, where $<K_d(\lambda)>_1$ can be derived from $R_{rs}(\lambda)$. This formulation thus ensures the applicability of the model in the context of ocean color remote sensing with one primary input of satellite-derived $R_{rs}(\lambda)$. The logical flow of the model, including each major step of the computations, is listed in Table 1. The key aspects of model formulation and parameterization are described below.

In general, the estimation of IOPs in the LS2 model is based on relationships between IOPs and AOPs, which are similar to those proposed in LS1 but R_{rs} is here used instead of $R(0^-)$:

$$b_b/\langle K_d\rangle_1 = f(R_{rs}) \tag{6}$$

$$\langle K_d\rangle_1/a = g(R_{rs}) \tag{7}$$

where the functions f and g depend on the ratio of molecular scattering to total scattering, η, and sun zenith angle, θ_s, or equivalently μ_w. These relationships are formulated irrespective of light wavelength so λ

Table 1
The Logical Flow of the LS2 Inverse Reflectance Model

Steps	Description of each step of the model
Step 1	$R_{rs}(\lambda)$ and the sun zenith angle, θ_s, are the input parameters of the model. μ_w is calculated from θ_s as $\mu_w = \cos[\text{asin}(\sin\theta_s/n_w)]$ where n_w is the refractive index of water with $n_w = 1.34$
Step 2	$<K_d(\lambda)>_1$ is obtained from in situ measurements when available, or from the neural network algorithm, which requires $R_{rs}(\lambda)$ as input parameter (in this case the inversion of $<K_d(\lambda)>_1$ at one given wavelength, requires $R_{rs}(\lambda)$ at several visible bands). Regional or other specific $<K_d(\lambda)>_1$ algorithms can also be used if deemed appropriate
Step 3	*Chl* is estimated from OC4v4 algorithm (O'Reilly et al., 2000) to obtain a rough proxy of $b_p(\lambda)$ using calculations based on Loisel and Morel (1998) and Morel and Maritorena (2001). The total scattering coefficient is then calculated as $b_p(\lambda) + b_w(\lambda)$, where the user can use the most appropriate spectral values for $b_w(\lambda)$. Other *Chl* algorithms can also be used if deemed appropriate
Step 4	$\eta(\lambda)$ is calculated as $b_w(\lambda)/b(\lambda)$
Step 5	$a(\lambda)$ is calculated from $R_{rs}(\lambda)$, $<K_d(\lambda)>_1$, $\eta(\lambda)$, and μ_w from equation (9) where the different coefficients are provided in a look-up table
Step 6	$a_{nw}(\lambda)$ is obtained by subtracting $a_w(\lambda)$ from $a(\lambda)$. As the model is free of spectral assumptions, the user can use the most appropriate spectral values for $a_w(\lambda)$
Step 7	$b_b(\lambda)$ is calculated from $R_{rs}(\lambda)$, $<K_d(\lambda)>_1$, $\eta(\lambda)$, and μ_w from equation (8) where the different coefficients are provided in a look-up table
Step 8	$b_{bp}(\lambda)$ is obtained by subtracting $b_{bw}(\lambda)$ from $b_b(\lambda)$, where $b_{bw}(\lambda)$ equals to half of the $b_w(\lambda)$ value used in Steps 3 and 4
Step 9	The remote-sensing reflectance corrected for Raman scattering contribution is obtained as a product of $\kappa(\lambda)$ and $R_{rs}(\lambda)$, where $\kappa(\lambda)$ is provided in a look-up table as a function of $b_b(\lambda)/a(\lambda)$. This new reflectance value is then used in Step 1, and the whole process is repeated until a convergence for successive estimates of IOPs is achieved

Note. The computer code of the inverse reflectance model is available on the IOCCG website htpp:www.ioccg.org/software/.

is omitted for brevity. Loisel and Stramski (2000) found that log-transformed data of $b_b/<K_d>_1$ are approximately linearly related to log-transformed data of $R(0^-)$, and an empirical relationship between these two quantities was established as a function of η and μ_w (equation (2)). Further analysis conducted in this study resulted in the formulation of a polynomial relationship between b_b, $<K_d>_1$, and R_{rs}:

$$b_b = \langle K_d \rangle_1 \left[b_{b1}(\eta, \mu_w) R_{rs} + b_{b2}(\eta, \mu_w) R_{rs}^2 + b_{b3}(\eta, \mu_w) R_{rs}^3 \right] \quad (8)$$

This type of relationship is similar to that used in Gordon et al. (1975), except that the b_{b1}, b_{b2}, and b_{b3} coefficients in our model are not constant but vary as a function of η and μ_w. A look-up table provides the values for b_{b1}, b_{b2}, and b_{b3} for different values of η and μ_w. An interpolation procedure is applied to calculate these coefficients for intermediate values of η and μ_w that are not included in the look-up table.

A comparison between the polynomial function (equation (8)) and the previously established relationship (equation (2)), in which $R(0^-)$ has been converted to R_{rs} according to Loisel et al. (2001b), is shown in Figure 1 where $b_b/<K_d>_1$ is plotted as a function of R_{rs} for different values of η and θ_s. For relatively low R_{rs} values (i.e., $R_{rs} < 0.01$ sr^{-1}) that encompass a broad range of marine environments with the exception of very oligotrophic waters for the blue and very turbid waters for the green and red parts of the spectrum, the agreement between the two approaches is good regardless of θ_s and η, i.e., also regardless of the shape of total scattering phase function. The agreement between these two fitting approaches tends, however, to deteriorate with an increase in R_{rs}. The polynomial fit (equation (8)) is clearly superior to the power function fit (equation (2)) for relatively large values of R_{rs}, as indicated by much closer agreement between the data points and the polynomial fit compared with the power function fit.

The absorption coefficient is estimated through a different formulation than in LS1. In LS1 the dependence of h on η was neglected (see the denominator of equation (1), and equation (3)). However, as noted in Loisel and Stramski (2000, see their Figure 2), h exhibits a slight dependency on η, especially for low values of η that are observed in turbid waters and also in clear waters for the green and red parts of the spectrum. In this study, we carried out further analysis to account for this dependence. As a result, a polynomial relationship has been established between a, $<K_d>_1$, and R_{rs}:

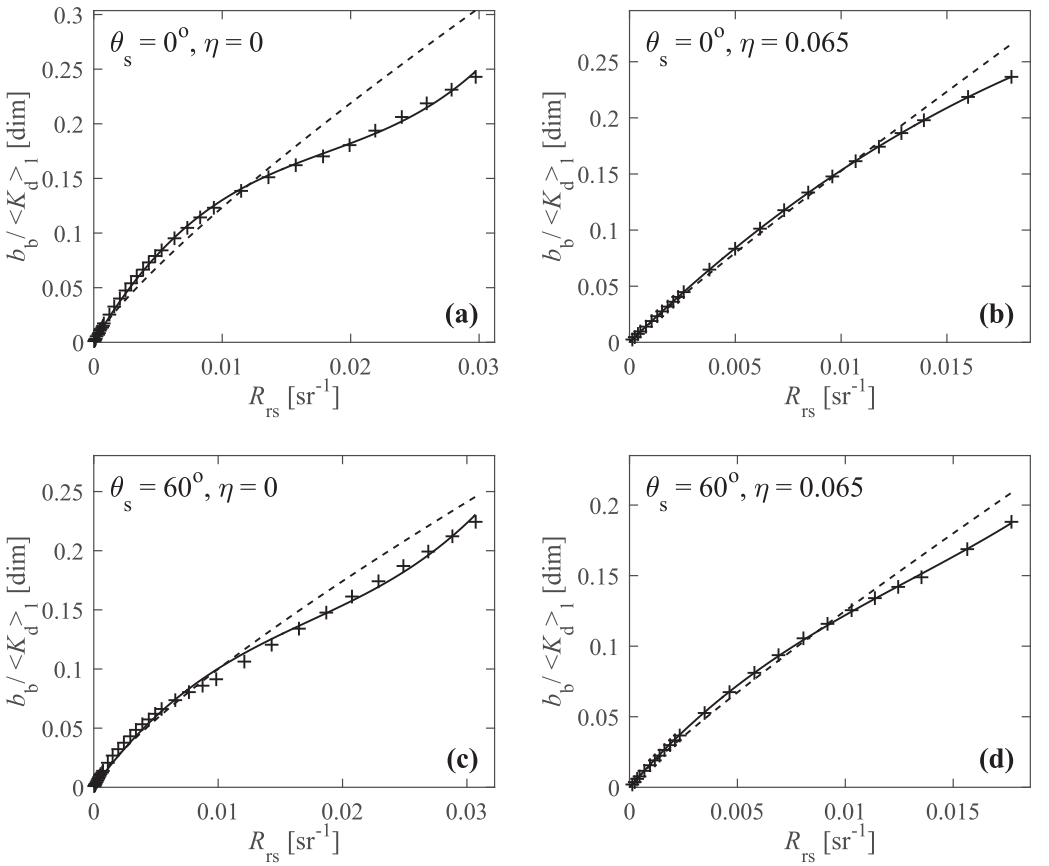

Figure 1. Relationship between $b_b/\langle K_d\rangle_1$ and R_{rs} for two different sun zenith angles, θ_s, and two different η values, as indicated. The crosses represent results from radiative transfer simulations, solid curves the polynomial relationship from the LS2 model (equation (8)), and dotted curves the relationship from the LS1 model (equation (2)) after converting $R(0^-)$ into R_{rs} as described in Loisel et al. (2001b).

$$a=\langle K_d\rangle_1/\left[a_1(\eta,\mu_w)+a_2(\eta,\mu_w)R_{rs}+a_3(\eta,\mu_w)R_{rs}^2+a_4(\eta,\mu_w)R_{rs}^3\right] \quad (9)$$

where the coefficients a_1, a_2, a_3, and a_4 depend on both η and μ_w and are provided in a look-up table. When R_{rs} tends toward 0, the ratio $a/\langle K_d\rangle_1$ approaches its limiting value given by μ_w that approximates the average cosine of near-surface light field under the conditions of radiative transfer simulations. A comparison of this new polynomial parameterization described by equation (9) with an earlier parameterization used in LS1 is provided in Figure 2. A polynomial parameterization results in improvement for low η and high R_{rs} values regardless of the sun angle, as indicated by closer agreement between the data points and the polynomial fit compared with the power function fit. The content of look-up tables with the values for the coefficients b_{b1}, b_{b2}, and b_{b3} involved in equation (8) and the coefficients a_1, a_2, a_3, and a_4 involved in equation (9) are provided in the supporting information.

In the LS1 model, the accuracy of the estimation of η is dependent on the accuracy of the estimation of total scattering coefficient b, which in turn depends largely on the nature and properties of particulate assemblages (Loisel & Stramski, 2000). The natural variability of particle properties will thus limit these accuracies. In this study, several approaches to improve the estimation of η were tested. Based on these analyses, we found that the use of a simple empirical formula between the particulate scattering coefficient, b_p, and *Chl* (Loisel & Morel, 1998) offers the best approach for estimating η. The spectral dependency of b_p is calculated according to Morel & Maritorena (2001), and *Chl* is estimated from R_{rs} using the standard OC4v4 algorithm (O'Reilly et al., 1998, 2000). No significant changes have been observed in the IOP retrieval accuracy when LS2 uses the OC4v6 algorithm instead of OC4v4 algorithm to calculate η. We also note that, in general, the use of *Chl* algorithm as part of the LS2 model is not limited to any specific *Chl* algorithm, as the users of LS2 can choose any version of *Chl* algorithm that is deemed most suitable. Although the b_p versus *Chl*

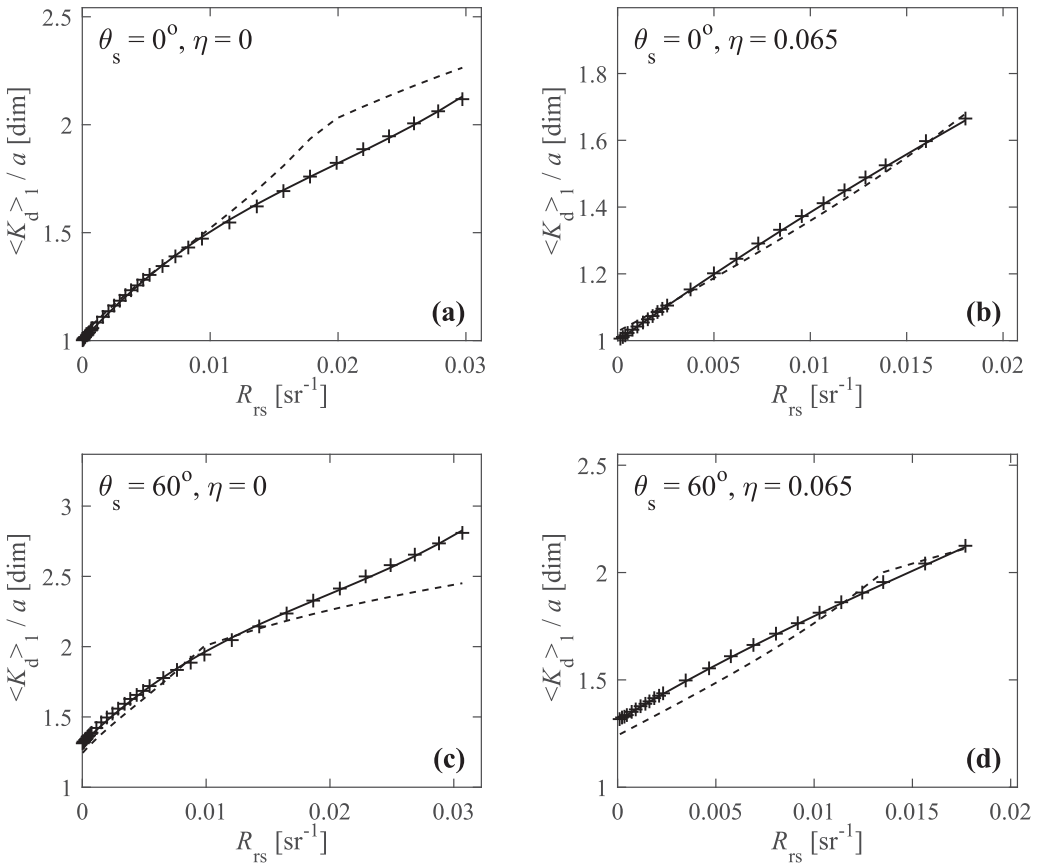

Figure 2. Relationship between $<K_d>_1/a$ and R_{rs} for two different sun zenith angles, θ_s, and two different η values as indicated. The crosses represent results from radiative transfer simulations, solid curves the polynomial relationship from the LS2 model (equation (9)), and dotted curves the relationship from the LS1 model (equation (1)) after converting $R(0^-)$ into R_{rs} as described in Loisel et al. (2001b).

relationship is known to underestimate b_p in coastal waters and the OC4v4 algorithm is generally not adequate for such waters, this simple approach provides relatively good estimates of η even in coastal waters. This can be explained by the fact that the underestimation of b_p is partly compensated by the overestimation of *Chl* in relatively turbid waters (Loisel et al., 2010).

Because η is involved in different formulas of the LS2 model as a second-order parameter, this simple approach for its estimation is deemed adequate for this model. Based on the analysis of synthetic data set DS1 (see section 4.1), from which the true η values can be calculated, we found that the present methodology can assess η from *Chl* with a root-mean-square-deviation (RMSD) value of 0.007 over a broad range of optical water types. This relatively good retrieval accuracy of η, as well as the fact that η is only a second-order parameter in LS2, explain why the performance of the model, as characterized by different statistical indicators (see section 4.2), is similar regardless of whether the true or modeled η values are used in LS2 (the statistical indicators vary less than 1% between these two versions).

The formulation of the LS2 model also involves the dependence of the relationships linking the AOPs with IOPs on the geometry of illumination of the ocean surface. This dependence is parameterized in terms of sun zenith angle, θ_s, or equivalently μ_w, and is meant to be representative primarily of clear sky conditions in the context of remote-sensing applications. It is important to note, however, that in clear waters the underwater light field in the near-surface ocean is dominated by single scattering events. In addition, the surface illumination conditions, as well as the viewing geometry in the case of remote-sensing observations when upwelling radiance is not necessarily measured along the vertical direction, may have potentially significant effect on the relationships linking $R_{rs}(\lambda)$ (or $<K_d(\lambda)>_1$) with IOPs, including clear sky conditions. These factors may result in a nonnegligible source of model uncertainty in clear waters. Note also that whereas the sun zenith angle involved as an input parameter to the model is meant to account for the

effect of different illumination conditions under clear skies, it can be inadequate to parameterize the complex illumination conditions at the ocean surface in the presence of clouds. This aspect must be recognized when the model is validated with in situ data that were collected under various sky conditions.

The equations of the LS2 model described above were developed for the hypothetical ocean scenario in the absence of Raman scattering. Therefore, the contribution of Raman scattering must be removed from the input data of R_{rs} (e.g., the satellite-derived R_{rs}) in order to ensure the best possible estimates of IOPs from the model. For this purpose, we use a similar iterative approach as in Loisel and Stramski (2000). Specifically, the Raman contribution to the measured data of spectral $R_{rs}(\lambda)$ that are used as input to the model is estimated in terms of the ratio of the hypothetical reflectance that would be measured in the absence of Raman scattering to the measured reflectance in the presence of both elastic scattering and Raman scattering. The values for this ratio, denoted as $\kappa(\lambda)$, were predetermined as a function of b_b/a within a wavelength range from 400 to 700 nm with a step of 4 nm, using radiative transfer calculations as described in Loisel and Stramski (2000). The $\kappa(\lambda)$ values are stored in a look-up table (see supporting information). The use of this look-up table as part of the iterative scheme to correct for Raman scattering is the last computational step that yields the final model-derived estimates of IOPs (see Table 1).

3.3. Estimation of Irradiance Attenuation Coefficient

In addition to $R_{rs}(\lambda)$, the diffuse attenuation coefficient for downwelling irradiance, $<K_d(\lambda)>_1$, is another AOP required to run the inverse LS2 model. The algorithm of Jamet et al. (2012) based on a neural network approach allows estimations of $<K_d(\lambda)>_1$ at any light wavelength between 412 and 670 nm from $R_{rs}(\lambda)$. This algorithm, which has been developed for ocean color remote-sensing applications, requires the input of $R_{rs}(\lambda)$ values at all standard bands in the visible spectral range of satellite ocean color sensors. While this approach provides better performance than previous methods (see Jamet et al., 2012), including the method used in LS1, the estimates of $<K_d(\lambda)>_1$ in optically very clear and very turbid waters are still not quite satisfactory.

A modified version of the Jamet et al. (2012) algorithm is used in this study to address this issue. This improved version is based on the same training data set and the use of the same training protocol as in Jamet et al. (2012). Similar to studies by Zhang and Fell (2007) and Wang et al. (2009), we utilize switch criteria to better address the transition between oligotrophic and turbid waters. The architecture of this new neural network has been also slightly modified compared to the original version of Jamet et al. (2012). Specifically, if the reflectance band ratio $R_{rs}(490)/R_{rs}(555)$ is lower or equal to 0.85, the neural network algorithm utilizes all $R_{rs}(\lambda)$ values between 443 and 670 nm as input parameters. In this case, the neural network has two hidden layers with five neurons for each layer. In contrast, if the reflectance ratio is higher than 0.85, the neural network algorithm does not take into account the red spectral band of $R_{rs}(\lambda)$ as input parameter. The choice to ignore the red band for clear waters is motivated by its generally low signal and low signal-to-noise ratio compared to other visible bands (e.g., Hu et al., 2012). In the case of $R_{rs}(490)/R_{rs}(555) > 0.85$, the neural network has two hidden layers with four neurons for each layer. For both cases of neural network inversion, the output of $<K_d(\lambda)>_1$ is generated for any wavelength between 412 and 670 nm, and in each case the algorithm architecture combines a minimal error with a minimal number of neurons. We also note that this neural network algorithm does not use $R_{rs}(412)$ as input because satellite-derived estimates of this reflectance are potentially subject to significant uncertainty, especially in coastal areas (Goyens et al., 2013; Jamet et al., 2011; Melin et al., 2007; Zibordi et al., 2006).

4. Model Evaluation and Validation

4.1. Synthetic, In Situ, and Match-up Data Sets

Four data sets consisting of relevant AOPs and IOPs are used to evaluate and validate the LS2 model. The first data set, referred to as DS1, consists of synthetic data of AOPs that were generated through radiative transfer simulations with input of synthetic IOP data. DS1 was created as part of the IOCCG Working Group project on inverse bio-optical algorithms (IOCCG, 2006). As the synthetic data set is free of measurement errors, it allows evaluating the uncertainties of the LS2 model, which are associated solely with the algorithmic formulation of the model. The data set DS1 covers a large range of bio-optical properties of the water column. For example, the nonwater absorption coefficient at 440 nm, $a_{nw}(440)$, which represents a sum of phytoplankton, nonalgal particulate and CDOM contributions, ranges between 0.0095 and 3.17 m^{-1} with a

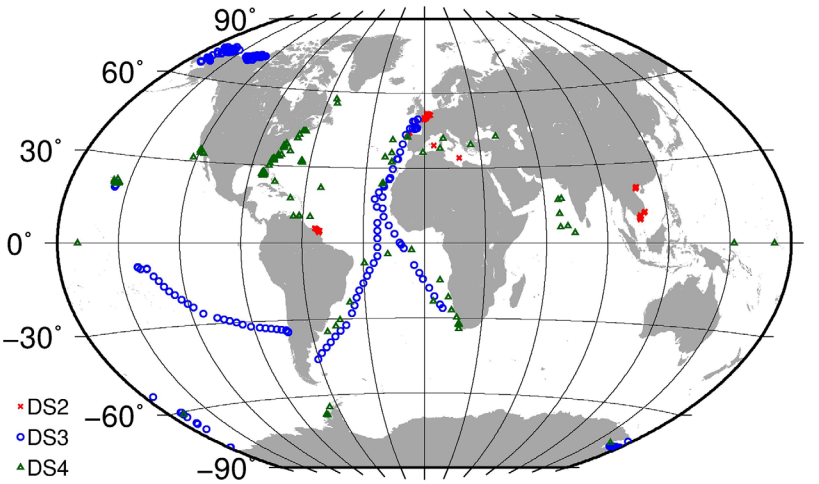

Figure 3. Location of oceanographic stations where in situ measurements were collected for creating data sets DS2, DS3, and DS4. Each data set is displayed with a different color as indicated.

median value of 0.216 m^{-1}. The particulate backscattering coefficient $b_{bp}(550)$ ranges between 0.0005 and 0.132 m^{-1} with a median value of 0.011 m^{-1}. Overall 500 IOP scenarios were used as input to generate DS1. For each set of input IOPs the simulations were made for three sun zenith angles of 0°, 30°, and 60°.

The second (DS2) and the third (DS3) data sets comprise in situ measurements collected in different oceanic and coastal environments (Figure 3), and span a broad range of trophic and environmental conditions (Figure 4). These data sets are used to validate the model for the scenario in which in situ measurements of R_{rs} provide input to the model. In this validation exercise, the model-derived IOPs are compared with in situ measurements of IOPs. Thus, this validation is subject to uncertainties in both the algorithmic formulation of the model and measurements of R_{rs} and IOPs. For a few reasons, we use DS2 and DS3 as two separate data sets, rather than one combined data set, in our model validation analysis. First, data contained in these data sets were collected

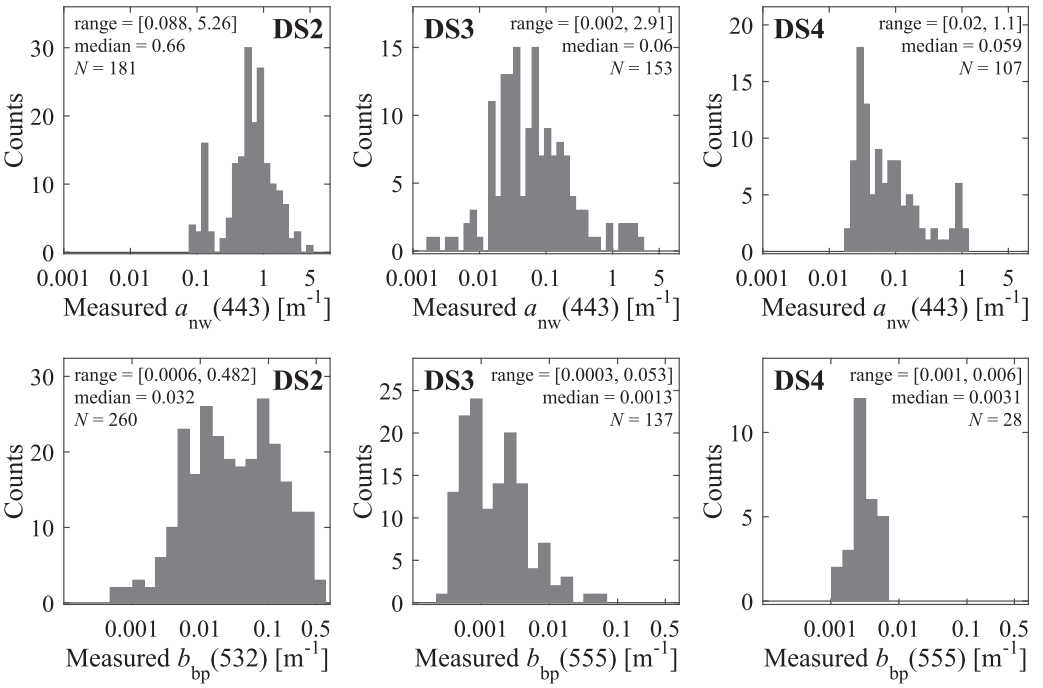

Figure 4. Histograms of in situ measurements of $a_{nw}(443)$ and $b_{bp}(532)$ or $b_{bp}(555)$ comprising the data sets DS2, DS3, and DS4. The minimum-to-maximum range and median values for the optical coefficients are indicated (in m^{-1}). *N* is the number of observations.

by different teams of investigators using different experimental approaches and instrumentation for measuring some optical quantities. Specifically, DS2 has been collected by the team of the Laboratory of Oceanography and Geoscience (LOG) in France and DS3 has been collected by the team of the Scripps Institution of Oceanography (SIO) in USA. Whereas each data set was collected with an internally consistent set of experimental approaches and protocols, there are some differences in that regard between the data sets. For instance, in DS2 the spectral nonwater absorption coefficient, $a_{nw}(\lambda)$, was obtained from in situ measurements with an ac-s instrument (WET Labs) as described in Neukermans et al. (2012). The absorption data in DS3 were obtained from spectrophotometric measurements made on discrete water samples, which provided the component absorption coefficients, $a_{CDOM}(\lambda)$ and $a_p(\lambda)=a_{ph}(\lambda)+a_{NAP}(\lambda)$, and hence, $a_{nw}(\lambda)=a_{CDOM}(\lambda)+a_p(\lambda)$ (e.g., Mitchell et al., 2003; Stramski et al., 2015). With regard to the backscattering coefficient, the ECO BB-9 and ECO-VSF sensors (WET Labs) have been used to measure $b_b(\lambda)$ in DS2, and Hydroscat-6 sensors (HOBI Labs) have been used in DS3. In both data sets, the determination of $b_{bp}(\lambda)$ was made by subtraction of pure water scattering contributions calculated using in situ measurements of water temperature and salinity. Another important reason for the use of separate data sets DS2 and DS3 in our model validation analysis is related to significant contrast between most data contained in DS2 and DS3 in terms of the coverage of diverse marine bio-optical environments. Specifically, DS2 is mainly dominated by Case 2 waters (Gordon & Morel, 1983; Morel & Prieur, 1977) in which the IOP variability is driven largely by dissolved and particulate matter of terrestrial origin, which is uncoupled with phytoplankton and associated material in the water column. DS2 comprises data collected in the English Channel and southern North Sea (Loisel et al., 2007; Lubac et al., 2008, Neukermans et al., 2012), French Guyana coastal waters (Loisel et al., 2009; Neukermans et al., 2012), Vietnam coastal waters (Loisel et al., 2017), and the Mediterranean Sea (Loisel et al., 2011). Only a small percentage of data (e.g., 9 out of 261 measurements of $b_{bp}(532)$) were collected in open ocean areas (Figure 3). Whereas the median values of $a_{nw}(443)=0.66\ m^{-1}$ and $b_{bp}(532)=0.032\ m^{-1}$ are relatively high, this data set covers a broad range of variability (Figure 4). The protocols for the determinations of IOPs and $R_{rs}(\lambda)$ in DS2 are described elsewhere (Loisel et al., 2007; Lubac et al., 2008, Neukermans et al., 2012).

DS3 comprises globally distributed data including polar and lower latitude regions and encompassing contrasting bio-optical environments that range from the clearest waters in ocean subtropical gyres to extremely turbid coastal waters (Figure 3). Data were collected during the Southern Ocean JGOFS program (Reynolds et al., 2001), the BIOSOPE project in the eastern South Pacific (Claustre et al., 2008; Stramski et al., 2008), two Atlantic cruises (ANT23 and ANT26) spanning low to midlatitudes (Stramski et al., 2008; Uitz et al., 2015), and the MALINA and ICESCAPE programs in Arctic waters (Neukermans et al., 2016; Reynolds et al., 2016). Additional data were collected at nine stations in Pacific waters off Hawaii. A description of measurement protocols for most of these cruises is provided in Stramski et al. (2008) and Zheng et al. (2014). For this study, most data in DS3 were reprocessed in the same manner to ensure consistency between the various field campaigns. In some cases, for example, the absorption data from the BIOSOPE cruise, the original data provided by investigators who made the relevant measurements are included in the DS3 data set without further reprocessing. Although DS3 includes some coastal stations, it is mainly representative of open ocean waters. The median values of $a_{nw}(443)=0.064\ m^{-1}$ and $b_{bp}(532)=0.0011\ m^{-1}$ are lower by one order of magnitude compared with DS2 (Figure 4). Also, both the lower and upper limits of the range in the IOPs are much smaller for DS3 compared with DS2. This comparison reflects significant contrast and complementarity of these two data sets.

The fourth data set (DS4) is derived from version 1.3.sv of the NASA bio-Optical Marine Algorithm Dataset (NOMAD, see Werdell & Bailey, 2005) which includes match-up data of $R_{rs}(\lambda)$ from satellite observations with Sea-viewing Wide Field-of-View Sensor (SeaWiFS) and coincident and colocated in situ measurements of IOPs. The nominal temporal and spatial thresholds used for specifying match-up criteria are ± 3 h and 0.1°, respectively. These criteria are met for 25 $b_{bp}(\lambda)$ data points out of 28, and for 72 $a_{nw}(\lambda)$ data points out of 107 in the data set. The remaining data points exhibit slightly higher spatial variability than the threshold value. The DS4 data set is used to validate the model for the scenario of remote-sensing application, in which satellite-derived R_{rs} provides input to the model. In this validation analysis, the model-derived IOPs are compared with in situ measurements of IOPs that are coincident and colocated with satellite-derived R_{rs}. Thus, this validation is subject to various uncertainties including the algorithmic formulation of the model, satellite derivation of R_{rs}, in situ measurements of IOPs, as well as spatial and temporal mismatch between the satellite and in situ observations. DS4 covers a broad range of open ocean and coastal environments (Figure 3). In this data set, the median values of $a_{nw}(443)=0.059\ m^{-1}$ and $b_{bp}(532)=0.0031\ m^{-1}$ are similar to those in DS3.

We also assembled an additional data set (DS5) of in situ radiometric measurements to validate the modified neural network algorithm for estimating $<K_d(\lambda)>_1$ from $R_{rs}(\lambda)$. This data set was not used in the development and training of the algorithm. DS5 includes data from the European coastal waters sampled as part of the Coastal Surveillance Through Observation of Ocean Color (COASTlOOC) project (Doron et al., 2007) as well as data collected in the Arabian Sea (Lee et al., 2005). Whereas the COASTlOOC data set is characterized by relatively high attenuation of light within the upper water column ($<K_d(490)>_1 = 0.464 \pm 0.640\ m^{-1}$), the Arabian Sea data set represents relatively clear waters ($<K_d(490)>_1 = 0.0445 \pm 0.0866\ m^{-1}$), which makes these two data sets complementary.

4.2. Statistical Indicators of Model Performance

To assess model performance, we use the graphical comparison of model predictions and observations as well as quantitative statistical metrics of differences between the corresponding model predictions and observations. We calculated several statistical indicators that are typically utilized in the assessment of model accuracy or skill in ocean sciences, including ocean color-related models (e.g., Brewin et al., 2015; Friedrichs et al., 2009; IOCCG, 2006; Stow et al., 2009). These indicators include the root-mean-square deviation, $RMSD_{log}$ and $RMSD$, calculated in the logarithmic and linear space, respectively:

$$RMSD_{log} = \left(\frac{\sum_{i=1}^{N} \left(log\left(IOP_i^{mod}\right) - log\left(IOP_i^{obs}\right)\right)^2}{N} \right)^{1/2} \tag{10}$$

$$RMSD = \left(\frac{\sum_{i=1}^{N} \left(\left(IOP_i^{mod}\right) - \left(IOP_i^{obs}\right)\right)^2}{N} \right)^{1/2} \tag{11}$$

where N is the number of data points, IOP^{mod} is the model-derived value of IOP, and IOP^{obs} is the known IOP value that was either measured in situ (data sets DS2, DS3, DS4) or assumed a priori as input to radiative transfer simulations (data set DS1).

We also report on the mean bias, MB, representing the difference between the means of the two data sets, i.e., untransformed model-derived data and corresponding untransformed measured data. MB is a component of total $RMSD$. Other indicators reported for untransformed data sets include the Pearson correlation coefficient, r, the median ratio of model-derived to measured values, MR, which provides a nondimensional measure of bias including its sign, and the median absolute percent difference, $MAPD$, calculated as the median of the individual absolute percent differences between the modeled and measured data.

We note that the calculation of statistical metrics for log-transformed data is generally recommended for data sets that are approximately log-normally distributed, which is often expected for bio-optical data (Campbell, 1995). We examined the probability distribution of IOPs in our data sets and found that the distribution of IOPs is variable, in some cases showing a bimodal distribution shape (see Figure 4), so a log-normal distribution does not necessarily provide an adequate approximation. Therefore, we report on statistical metrics calculated in both the logarithmic and linear space. In addition to calculating $RMSD_{log}$, type-II linear regression analysis for model-derived versus observed data was also performed on log-transformed data (Laws, 1997; Legendre & Legendre, 1998). We provide examples from this regression analysis including the values of the Pearson correlation coefficient, r_{log}, for the log-transformed data.

The results of model performance analysis involving the use of synthetic, in situ, and match-up data sets are presented below. These results were obtained for the light wavelengths of 412, 443, 490, 510, 555, and 670 nm (if available), which correspond to the center or near-center wavelengths of typical visible bands on satellite ocean color sensors.

4.3. Evaluation of $<K_d(\lambda)>_1$ Derived From Neural Network Algorithm

To evaluate the estimation of $<K_d(\lambda)>_1$ from the modified neural network algorithm, in situ measurements of $R_{rs}(\lambda)$ are used as input to the algorithm and the algorithm-derived $<K_d(\lambda)>_1$ is compared with in situ measurements of $<K_d(\lambda)>_1$ (Figure 5). This analysis utilizes the field data set DS5. As shown for an example

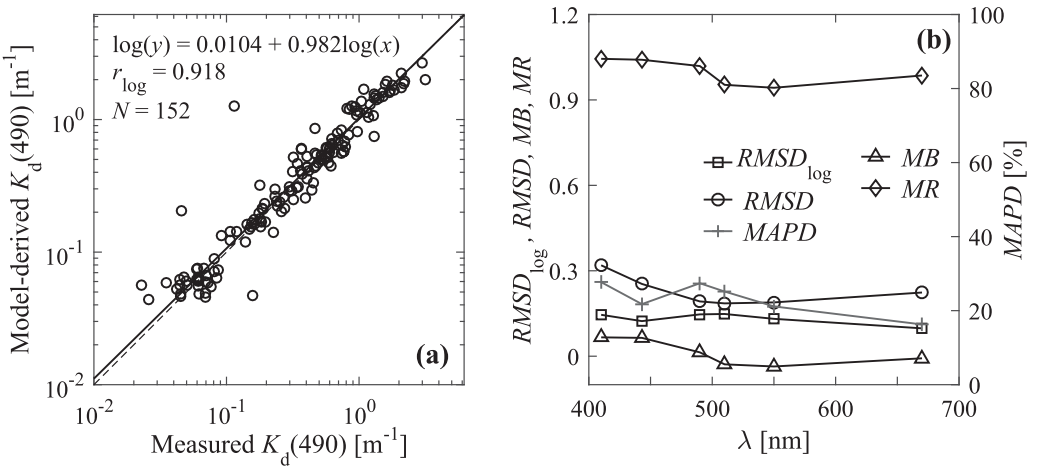

Figure 5. (a) Comparison of the model-derived and measured $<K_d(490)>_1$ values. The modified neural network algorithm, which has been implemented into the LS2 model, was used to derive $<K_d(490)>_1$. The solid line represents the best fit linear regression type-II fit to log-transformed data and the dashed line represents the 1:1 line. The regression equation (where x is the abscissa and y the ordinate), values of the Pearson correlation coefficient for log-transformed data r_{log}, and the number of data points N are displayed. (b) Spectra of statistical indicators calculated for the data of model-derived versus measured $<K_d(490)>_1$ values (see text for details).

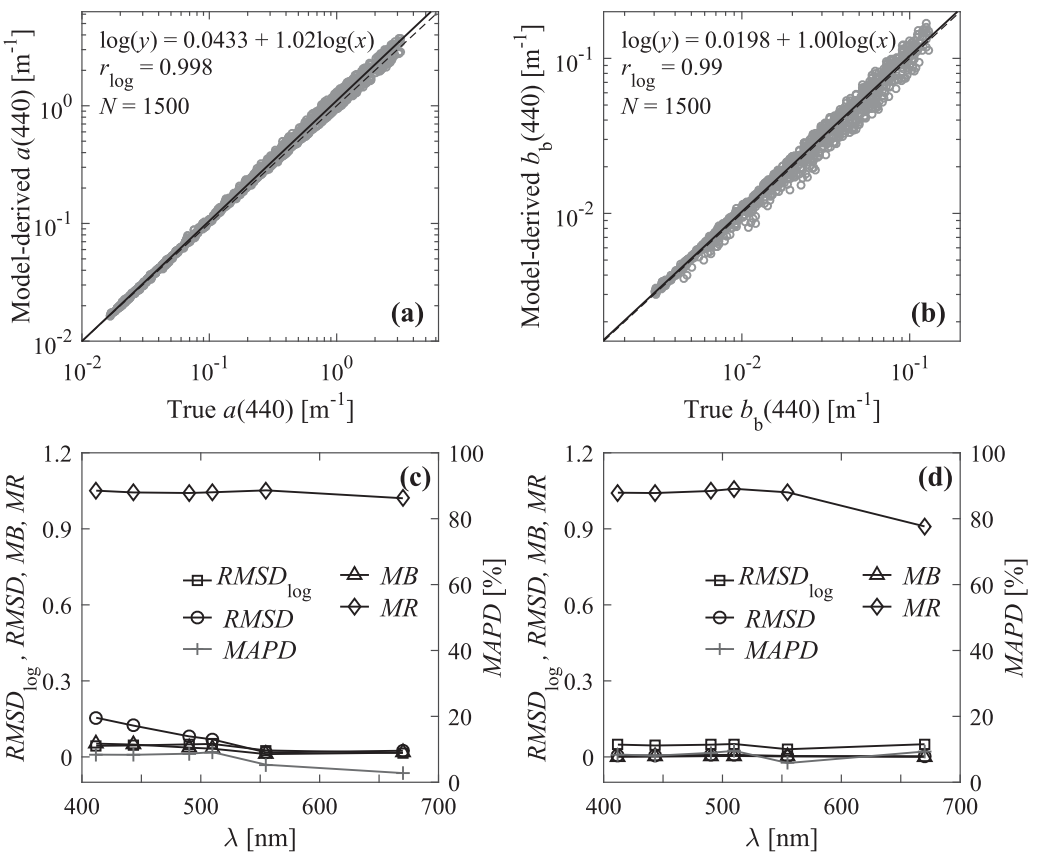

Figure 6. (a) Comparison of model-derived and reference (true) absorption coefficient, $a(440)$, for the synthetic data set DS1. The LS2 model was run with inputs of $<K_d(\lambda)>_1$ and $R_{rs}(\lambda)$. The solid line represents the best fit linear regression type-II fit to log-transformed data and the dashed line represents the 1:1 line. The regression equation (where x is the abscissa and y the ordinate), values of the Pearson correlation coefficient for log-transformed data r_{log}, and the number of data points N are displayed. (b) Same as (a) but for the backscattering coefficient $b_b(\lambda)$. (c) Spectra of statistical indicators calculated for the data of model-derived versus measured $a(\lambda)$ values (see text for details). (d) Same as (c) but for $b_b(\lambda)$.

wavelength of 490 nm, a very good performance of the algorithm is achieved over the whole range of $<K_d(490)>_1$ values that span two orders of magnitude (Figure 5a). For example, at this wavelength the slope, *S*, of the best fit regression line between the log-transformed data is 0.982, which is very close to 1, and the values for the statistical indicators of $RMSD_{log}$ and *RMSD* are 0.15 and 0.19 m^{-1}, respectively. This good retrieval accuracy is maintained over the most part of the visible spectrum (Figure 5b).

The performance of the present algorithm for estimating $<K_d(\lambda)>_1$ also compares favorably with the results obtained from the original algorithm of Jamet et al. (2012). The latter has shown better performance than previously published algorithms (see Figure 4 and Table 4 in Jamet et al., 2012). Compared to the Jamet et al. (2012) algorithm, the retrieval accuracy of $<K_d(\lambda)>_1$ using our new algorithm is considerably improved in the blue part of the spectrum and slightly improved in the green and red spectral regions (not shown). This improvement is more pronounced within the range of relatively high values of $<K_d(\lambda)>_1$. For example, at 410 nm where this range is characterized approximately by $<K_d(410)>_1$ exceeding 0.54 m^{-1}, the *RMSD* in the present algorithm is reduced to about 0.3 m^{-1} compared with 0.57 m^{-1} in the Jamet et al. (2012) algorithm.

4.4. Model Evaluation With Synthetic Data Set

The synthetic data set DS1 is free of measurement errors, allowing evaluation of the uncertainties of the inverse LS2 model, which are associated solely with the formulation of modeled relationships for calculating the IOPs given the input data of $R_{rs}(\lambda)$. In this analysis, the model-derived IOPs are compared with the synthetic data of IOPs that were used as input to radiative transfer simulations to create DS1. The IOPs tested include the coefficients of total backscattering, $b_b(\lambda)$, particulate backscattering, $b_{bp}(\lambda)$, total absorption, $a(\lambda)$, and nonwater absorption, $a_{nw}(\lambda)$. In terms of input data to the LS2 model, we evaluate two cases. First, the synthetic data of both $R_{rs}(\lambda)$ and $<K_d(\lambda)>_1$ generated by radiative transfer simulations are used as input to the model, so that in this case the neural network algorithm for estimating $<K_d(\lambda)>_1$ from $R_{rs}(\lambda)$ is

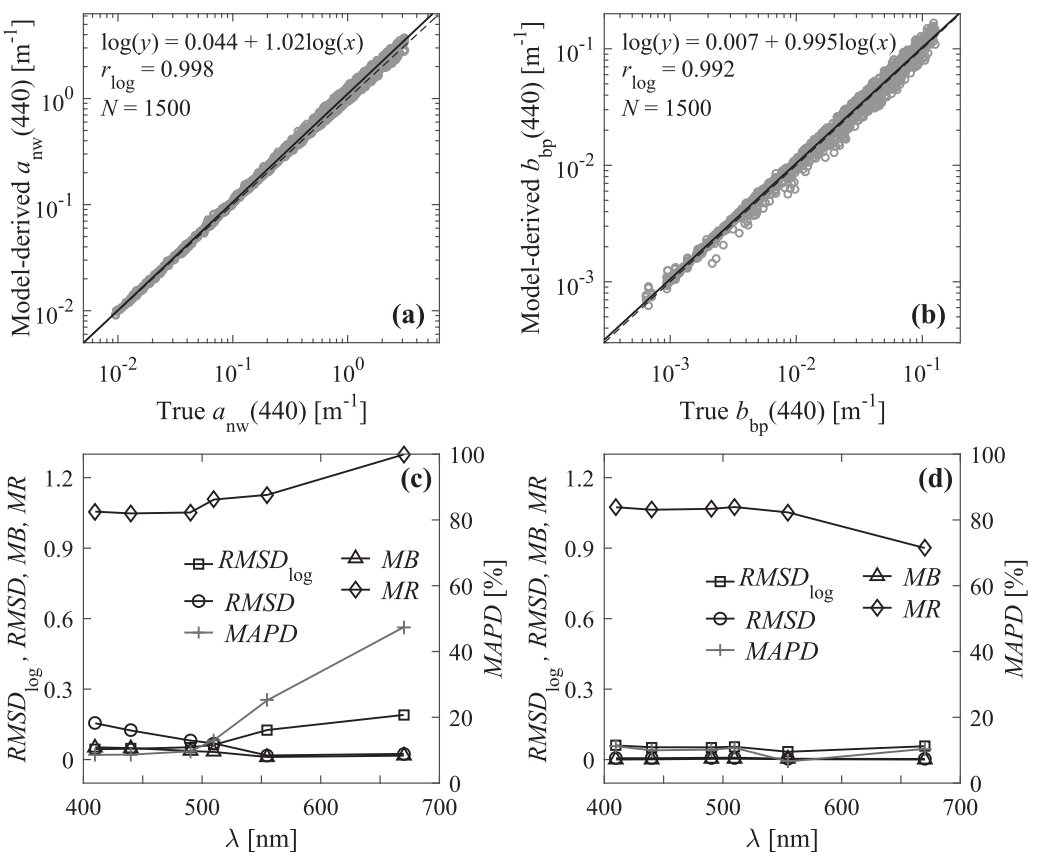

Figure 7. Same as Figure 6 but for the nonwater absorption coefficient, a_{nw} (plots (a) and (c)) and the particulate backscattering coefficient b_{bp} (plots (b) and (d)).

Table 2
Statistical Indicators of the Performance of the LS2 Model in Retrieving Nonwater IOPs at Selected Light Wavelengths, $a_{nw}(\lambda)$ and $b_{bp}(\lambda)$, for the DS1 Data Set

		N	r	$RMSD_{log}$	RMSD (m^{-1})	MB (m^{-1})	MR	MAPD (%)
DS1	$a_{nw}(410)$	1500	0.99	0.044	0.155	0.052	1.055	8.59
Both $R_{rs}(\lambda)$ and $<K_d(\lambda)>_1$ are	$a_{nw}(440)$	1500	0.99	0.046	0.124	0.049	1.048	8.65
used as input parameters	$a_{nw}(490)$	1500	0.99	0.052	0.081	0.037	1.052	9.66
	$a_{nw}(510)$	1500	0.99	0.063	0.069	0.032	1.107	13.07
	$a_{nw}(555)$	1500	0.99	0.126	0.018	0.011	1.127	25.18
	$a_{nw}(670)$	1500	0.99	0.190	0.024	0.017	1.300	47.40
	$b_{bp}(410)$	1500	0.99	0.060	0.006	0.0003	1.074	11.20
	$b_{bp}(440)$	1500	0.99	0.052	0.006	0.0011	1.063	9.96
	$b_{bp}(490)$	1500	0.99	0.052	0.008	0.0031	1.070	10.16
	$b_{bp}(510)$	1500	0.99	0.055	0.008	0.0036	1.075	10.71
	$b_{bp}(555)$	1500	0.99	0.033	0.004	0.0018	1.052	6.57
	$b_{bp}(670)$	1500	0.99	0.057	0.003	0.0001	0.901	10.40
DS1	$a_{nw}(410)$	1500	0.99	0.085	0.239	0.0481	1.056	16.73
Only $R_{rs}(\lambda)$ is used as	$a_{nw}(440)$	1500	0.99	0.076	0.159	0.0515	1.065	15.01
input parameter	$a_{nw}(490)$	1500	0.99	0.108	0.095	0.0407	1.183	23.36
	$a_{nw}(510)$	1500	0.97	0.213	0.076	0.0273	1.083	24.67
	$a_{nw}(555)$	1500	0.95	0.251	0.053	0.0199	1.227	55.55
	$a_{nw}(670)$	1500	0.74	0.644	0.094	0.0504	1.839	426.80
	$b_{bp}(410)$	1500	0.97	0.137	0.009	0.0006	1.027	22.73
	$b_{bp}(440)$	1500	0.98	0.100	0.008	0.0011	1.048	18.19
	$b_{bp}(490)$	1500	0.99	0.104	0.008	0.0034	1.165	21.99
	$b_{bp}(510)$	1500	0.99	0.104	0.008	0.0029	1.041	17.61
	$b_{bp}(555)$	1500	0.99	0.087	0.009	0.0033	1.080	16.98
	$b_{bp}(670)$	1500	0.99	0.104	0.007	0.0008	0.942	15.66

Note. All statistics were calculated in linear space except for $RMSD_{log}$ that was calculated for log-transformed data.

bypassed. Second, the synthetic data of $R_{rs}(\lambda)$ generated by radiative transfer simulations are the sole input to the model and $<K_d(\lambda)>_1$ is obtained from $R_{rs}(\lambda)$ using the neural network algorithm.

The first case of the evaluation analysis characterizes the performance of model formulation irrespective of the neural network algorithm for estimating $<K_d(\lambda)>_1$. Both $a(\lambda)$ (Figures 6a and 6c) and $b_b(\lambda)$ (Figures 6b and 6d) coefficients are derived with a very good accuracy for the entire range of examined light wavelengths and sun angles. The best fit regression lines of modeled versus observed data are very close to the 1:1 line with the values for the slope and the correlation coefficient very close to 1, as shown for the example wavelength of 440 nm (Figures 6a and 6b). The *MR* values of $a(\lambda)$ calculated for the whole data set DS1 are also very close to 1 (within 5%) regardless of wavelength, which indicates a very small bias. The mean bias, *MB*, for $a(\lambda)$ ranges between 0.01 m^{-1} at 670 nm and 0.05 m^{-1} at 412 nm (Figure 6c). The lower values of *MB* in the red can be attributed to the dominance of predictable and nearly constant contribution of pure water to total absorption in this spectral region. Similar good performance is observed for the retrieval of $b_b(\lambda)$, for which the *MR* and *MB* vary within the ranges 1.04–0.91 and 0.0001–0.003 m^{-1}, respectively (Figure 6d). The spectrally averaged values of *RMSD* and *MAPD* for $a(\lambda)$ are 0.078 ± 0.054 m^{-1} and 7.1%, respectively. For $b_b(\lambda)$ these values are 0.005 ± 0.002 m^{-1} and 8.3%.

At the wavelength of 440 nm, the best fit regression lines of modeled versus observed data for nonwater absorption coefficient, $a_{nw}(\lambda)$ and particulate backscattering, $b_{bp}(\lambda)$, coefficients are very close to the 1:1 line (Figures 7a and 7b). However, the retrieval accuracy of $a_{nw}(\lambda)$ is very good only for wavelengths from the blue and blue-green regions up to about 510 nm (Figure 7c). This good retrieval of $a_{nw}(\lambda)$ in this spectral region is comparable to that for $a(\lambda)$. The model performance for $a_{nw}(\lambda)$ deteriorates significantly for wavelengths of 555 and 670 nm as indicated by significant increase in $RMSD_{log}$, *MR*, and *MAPD* (Figure 7c and Table 2). This result is associated primarily with relatively poor performance of the model in clear ocean waters where molecular water is the dominant absorbing component and $a_{nw}(\lambda)$ has small contribution to $a(\lambda)$ within the long-wavelength portion of the spectrum. For example, within the data set DS1 pure seawater contributes about 99% to $a(670)$ and 95% to $a(550)$ in oligotrophic waters with $Chl < 0.1$ mg m^{-3}.

This makes it practically impossible to achieve consistently good estimation of $a_{nw}(\lambda)$ from an inverse reflectance model under such circumstances. The results for $b_{bp}(\lambda)$ indicate similar retrieval accuracy to that for $b_b(\lambda)$ (Figures 7b and 7d; Table 2), and the model performance is consistent over the entire dynamic range and spectral range of backscattering values. For example, the *MR* and *MB* values for $b_{bp}(\lambda)$ are within the range of 0.9–1.075 and 0.0001–0.0036 m^{-1}, respectively. The *MAPD* value averaged over the entire spectral region is 9.8%.

The second case of the model evaluation analysis with synthetic data set DS1 is focused on the influences of the neural network algorithm for estimating $<K_d(\lambda)>_1$ on the overall performance of the model. In this analysis, the $R_{rs}(\lambda)$ data are the sole input to the model and $<K_d(\lambda)>_1$ is obtained from $R_{rs}(\lambda)$ using the neural network algorithm. For $a(440)$ and $b_b(440)$ the regression line of modeled versus observed data are very close to the 1:1 line (Figures 8a and 8b) but the scatter of data around this line is larger compared with the results shown in Figure 6. This increase in data scatter is caused by uncertainties in the estimates of $<K_d(\lambda)>_1$. For instance, the $RMSD_{log}$ value for both $a(440)$ and $b_b(440)$ is about 0.07, which represents a 1.5-fold increase compared with the modeling case with the input of exact $<K_d(\lambda)>_1$. However, the values for the slope of the regression (not shown) and *MR* remain close to 1 for all wavelengths (Figures 8c and 8d). The *RMSD* values also remain relatively low, 0.16 m^{-1} for $a(440)$ and 0.007 m^{-1} for $b_b(440)$. The model estimation of $b_b(\lambda)$ is consistent across the whole spectrum with spectrally averaged *RMSD* and *MB* values of 0.008 ± 0.001 m^{-1} and 0.002 ± 0.001 m^{-1}, respectively. A similarly consistent spectral pattern holds for $a(\lambda)$ that is estimated with a mean *RMSD* and *MB* of 0.11 ± 0.07 m^{-1} and 0.035 ± 0.014 m^{-1}, respectively. For both $a(\lambda)$ and $b_b(\lambda)$, the *MAPD* value is around 15% regardless of wavelength (Figures 8c and 8d).

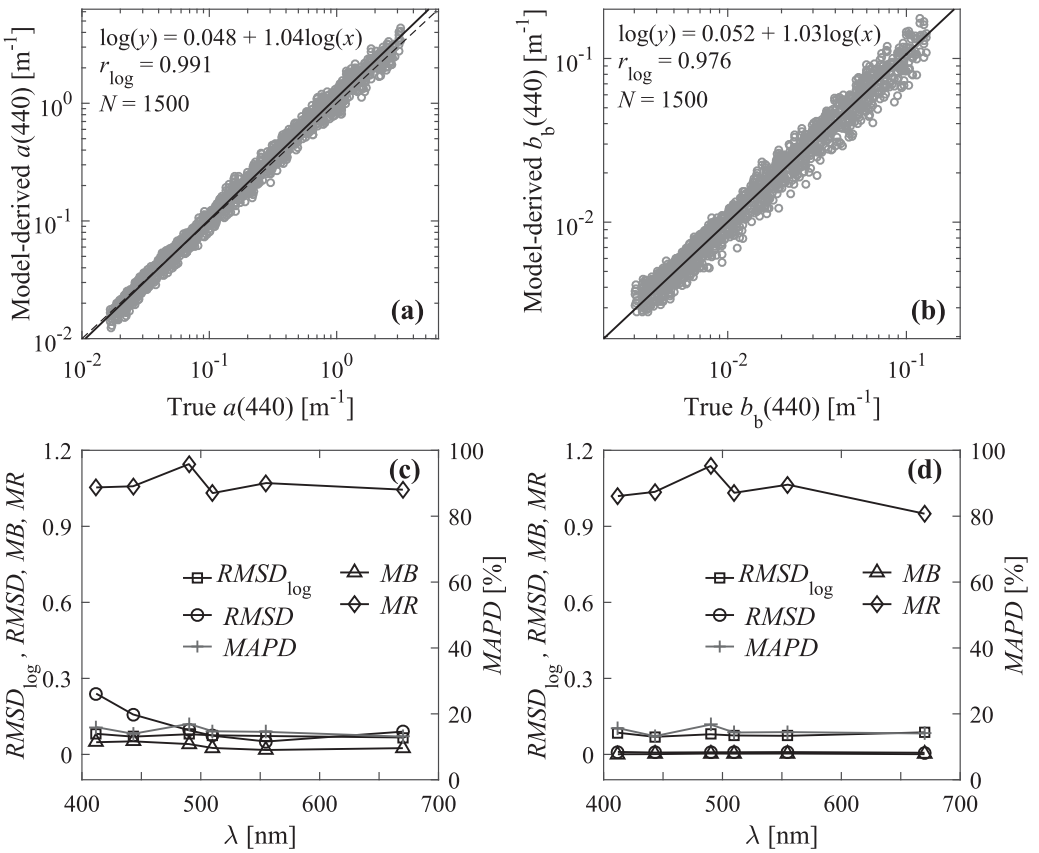

Figure 8. (a) Comparison of model-derived and reference (true) absorption coefficient, $a(440)$, for the synthetic data set DS1. The LS2 model was run with input of $R_{rs}(\lambda)$. The $<K_d(\lambda)>_1$ values were derived from the neural network algorithm that has been implemented into the LS2 model using $R_{rs}(\lambda)$ as input. The solid line represents the best fit linear regression type-II fit to log-transformed data and the dashed line represents the 1:1 line. The regression equation (where *x* is the abscissa and *y* the ordinate), values of the Pearson correlation coefficient for log-transformed data r_{log}, and the number of data points *N* are displayed. (b) Same as (a) but for the backscattering coefficient $b_b(\lambda)$. (c) Spectra of statistical indicators calculated for the data of model-derived versus measured $a(\lambda)$ values (see text for details). (d) Same as (c) but for $b_b(\lambda)$.

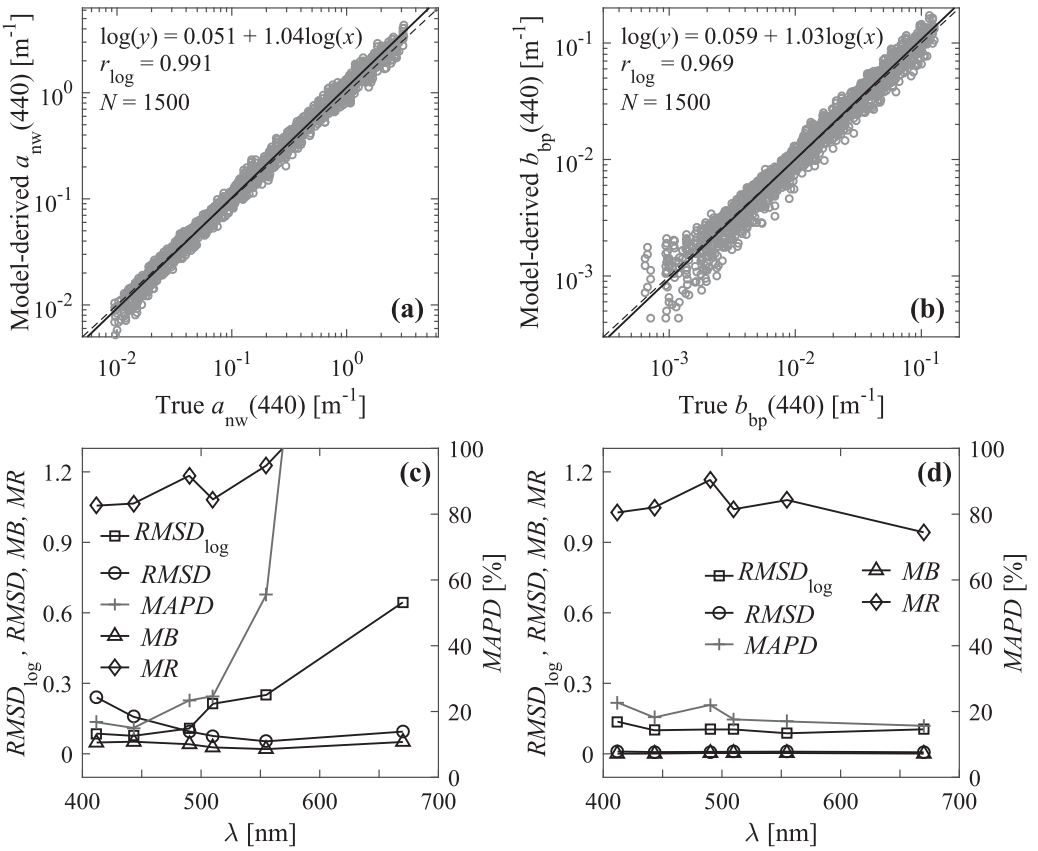

Figure 9. Same as Figure 8 but for the nonwater absorption coefficient, a_{nw} (plots (a) and (c)) and the particulate backscattering coefficient b_{bp} (plots (b) and (d)).

The retrieval of both $a_{nw}(440)$ and $b_{bp}(440)$ from the sole input of $R_{rs}(440)$ is also characterized by good statistical indicators of best fit regression and correlation between the modeled and observed data (Figures 9a and 9b; Table 2). However, the data scatter around the regression line is larger in Figures 9a and 9b compared with Figures 7a and 7b, which is attributable to uncertainties in the estimation of $<K_d(\lambda)>_1$. The retrieval of $a_{nw}(\lambda)$ deteriorates significantly for wavelengths longer than about 510 nm (Figure 9c and Table 2). This deterioration is more pronounced compared with the case shown in Figure 7c when both the exact (i.e., synthetic) $R_{rs}(\lambda)$ and $<K_d(\lambda)>_1$ were used as model inputs (see also Table 2). In contrast, the uncertainties in the estimation of $<K_d(\lambda)>_1$ have relatively weak effect on the performance of the model in terms of estimating $b_{bp}(\lambda)$ over the entire spectrum (Figure 9d and Table 2). This performance remains good although the statistical indicators deteriorated to some extent compared with the scenario when the exact $<K_d(\lambda)>_1$ serves as input to the model.

Using the synthetic data set DS1, we have also compared the performance of the LS2 model with the original LS1 model, as well as with the version of LS1 model that was used in the IOCCG (2006) study (Loisel & Poteau, 2006). In this comparison only the data for a sun zenith angle of 30° are taken into account. We found that the LS2 model provides the best retrievals of IOPs as evidenced by better statistical indicators for this model compared with earlier versions of LS1 (Figure 10).

4.5. Model Validation With In Situ Data Sets

The validation of model-derived results with in situ data sets is performed using $R_{rs}(\lambda)$ as the sole input parameter to the LS2 model. The two in situ data sets (DS2 and DS3) containing coincident measurements of $R_{rs}(\lambda)$ and IOPs are used for this validation. Whereas the radiative transfer simulations for the model development were conducted for clear skies with a main purpose of model applicability in remote-sensing context, the in situ data used in our analysis of model validation were often collected under cloudy skies.

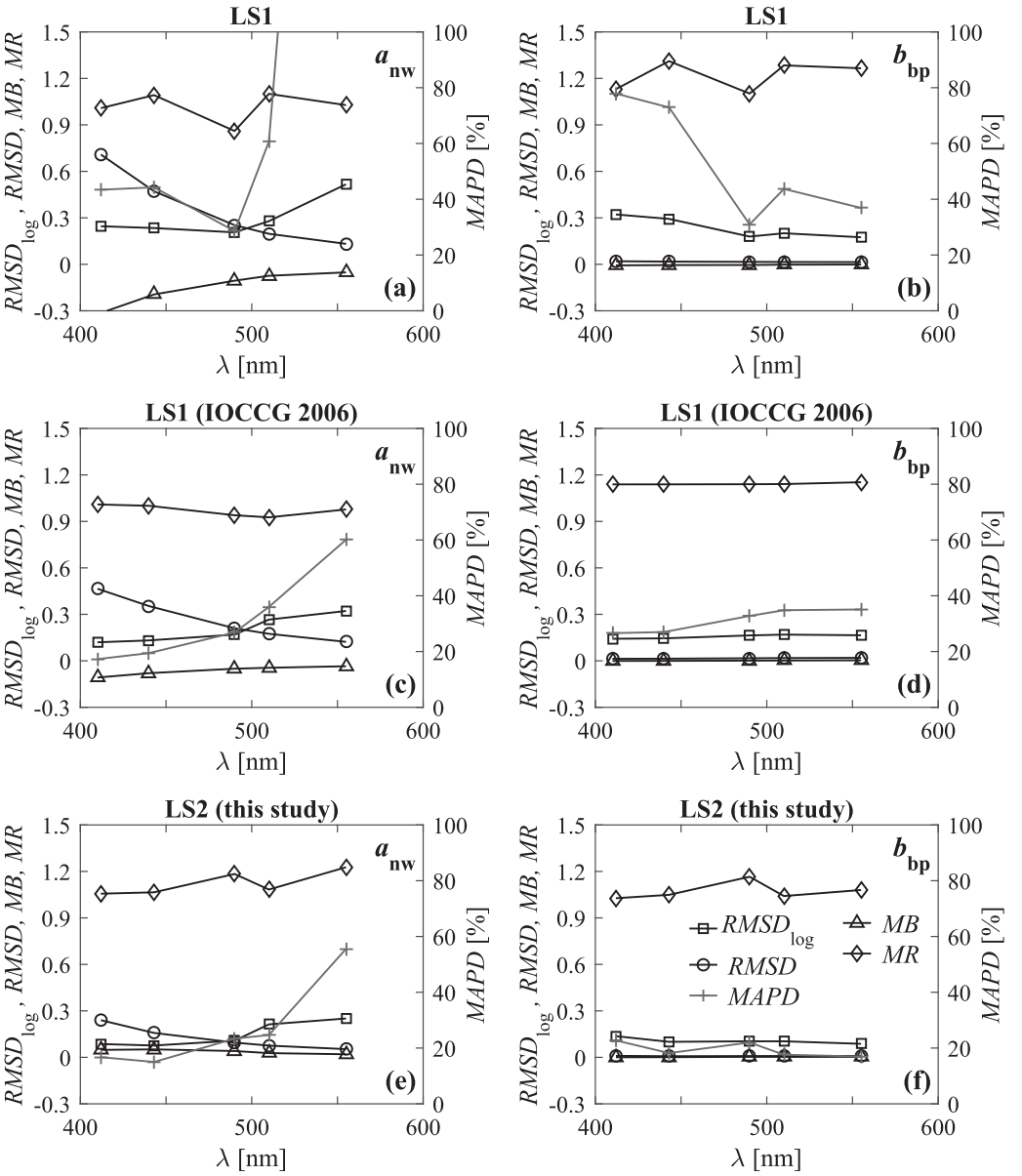

Figure 10. Spectra of statistical indicators calculated for the comparison of model-derived versus measured $a_{nw}(\lambda)$ values (plots (a), (c), and (e)) and model-derived versus measured $b_{bp}(\lambda)$ values (plots (b), (d), and (f)). The results are shown for: (a) and (b) the original LS1 model; (c) and (d) the modified version of LS1 from the 2006 IOCCG project, and (e) and (f) the LS2 model. Only data for the sun zenith angle of 30° have been considered in these results.

For a totally overcast sky, we found it reasonable to assume the sun zenith angle of 45° as input to the model. For partial cloud cover we used the actual sun angle during the in situ measurement as input to the model (which is the same approach as for clear skies). This assumption was based largely on the fact that comprehensive information on cloud cover and cloud types has not been consistently available during the field experiments to allow a development of more rigorous approach to account for the presence of clouds.

The comparative analysis of model-derived and measured values is performed for both the total and nonwater IOPs. The statistical indicators calculated on the basis of these comparisons at selected light wavelengths are presented for the total $a(\lambda)$ and $b_b(\lambda)$ in Table 3 and for $a_{nw}(\lambda)$ and $b_{bp}(\lambda)$ in Table 4. Graphical illustrations of this comparative analysis are shown for the nonwater IOPs, $a_{nw}(\lambda)$, and $b_{bp}(\lambda)$ (Figures 11–15).

Table 3
Statistical Indicators for the Performance of the LS2 Model in Retrieving Total IOPs at Selected Light Wavelengths, $a(\lambda)$ and $b_b(\lambda)$, Based on the Analysis of the DS2, DS3, and DS4 Data Sets

		N[a]	r	$RMSD_{log}$	$RMSD$ (m^{-1})	MB (m^{-1})	MR	$MAPD$ (%)
DS2	a (412)	170 (0)	0.80	0.156	0.433	0.114	1.117	25.77
	a (443)	170 (0)	0.81	0.147	0.322	0.059	1.029	22.76
	a (490)	170 (0)	0.78	0.158	0.221	0.003	0.996	22.25
	a (510)	170 (0)	0.74	0.171	0.197	−0.007	1.038	24.37
	a (555)	169 (0)	0.60	0.286	0.155	−0.008	1.107	31.33
	a (670)							
	b_b (412)							
	b_b (443)							
	b_b (490)	188 (0)	0.79	0.173	0.093	0.0136	1.202	30.34
	b_b (510)	183 (0)	0.83	0.165	0.077	0.0151	1.102	25.54
	b_b (532)	262 (0)	0.82	0.186	0.053	0.0035	0.996	27.03
	b_b (670)	258 (0)	0.70	0.259	0.049	0.0153	1.175	43.47
DS3	a (412)	153 (0)	0.92	0.113	0.251	0.0378	0.973	12.01
	a (443)	153 (0)	0.91	0.102	0.233	0.0417	0.978	14.27
	a (490)	150 (0)	0.85	0.098	0.174	0.0320	1.069	12.97
	a (510)	150 (0)	0.82	0.085	0.155	0.0209	0.966	12.01
	a (555)	147 (0)	0.77	0.069	0.102	0.0170	1.078	9.34
	a (670)	147 (0)	0.54	0.052	0.073	−0.0225	0.935	6.99
	b_b (412)							
	b_b (443)	165 (0)	0.90	0.108	0.002	0.0005	1.202	20.61
	b_b (490)							
	b_b (510)	161 (0)	0.94	0.103	0.002	0.0002	1.200	21.36
	b_b (555)	147 (0)	0.94	0.100	0.002	0.0001	1.166	18.44
	b_b (670)	96 (0)	0.96	0.186	0.001	−0.0001	0.943	25.80
DS4	a (412)	105 (0)	0.89	0.155	0.119	−0.0207	0.931	18.25
	a (443)	107 (0)	0.89	0.138	0.089	−0.0170	0.939	16.25
	a (490)	107 (0)	0.87	0.117	0.053	−0.0028	1.034	16.79
	a (510)	107 (0)	0.86	0.104	0.042	−0.0042	0.938	11.68
	a (555)	106 (0)	0.84	0.074	0.026	0.0053	1.045	8.56
	a (670)	99 (0)	0.39	0.064	0.072	−0.0026	0.964	7.93
	b_b (412)	28 (0)	0.35	0.179	0.002	−0.0004	0.919	19.51
	b_b (443)	28 (0)	0.53	0.101	0.001	0.0001	0.993	14.91
	b_b (490)	28 (0)	0.70	0.087	0.001	0.0003	1.101	15.85
	b_b (510)	28 (0)	0.73	0.081	0.001	0.0001	1.023	12.98
	b_b (555)	28 (0)	0.78	0.096	0.001	0.0006	1.172	17.64
	b_b (670)	28 (0)	0.66	0.249	0.001	−0.0002	0.900	32.91

Note. The statistics were calculated in linear space except for $RMSD_{log}$ that was calculated for log-transformed data. [a]The N value indicates the number of stations with both positive in situ and model-derived values, while the value in the parentheses indicates the number of stations with positive in situ measurements but negative model-derived values.

4.5.1. Comparisons for Predominantly Coastal Waters (DS2)

The data set DS2 is characterized by large variation in light absorption of seawater. For example, $a_{nw}(443)$ values vary over nearly two orders of magnitude from 0.088 to 5.26 m^{-1} with a median value of 0.663 m^{-1}. We note that for the considered light wavelengths between 412 and 555 nm the $a_{nw}(\lambda)$ values in DS2 are almost always much higher than $a_w(\lambda)$. The statistical indicators provided for $a(\lambda)$ and $a_{nw}(\lambda)$ in Tables 3 and 4, respectively, show that these absorption coefficients can be derived with good accuracy in coastal environments within the blue and green parts of the spectrum. The statistical indicators of model performance are similar for $a(\lambda)$ and $a_{nw}(\lambda)$. The model performance for $a_{nw}(\lambda)$ is also illustrated graphically in Figure 11. For example, the $RMSD_{log}$ values for $a(\lambda)$ range from 0.147 at 443 nm to 0.286 at 555 nm (Table 3). For $a_{nw}(\lambda)$ this error is similar, ranging from 0.150 at 443 nm to 0.248 at 555 nm (Table 4 and Figure 11d). Regardless of wavelength, the median ratio of modeled to measured values, MR, for $a(\lambda)$ and $a_{nw}(\lambda)$ are close to 1 (within ~10%). The mean bias, MB, assumes small positive values in the blue and small negative values in the green. For both $a(\lambda)$ and $a_{nw}(\lambda)$, the median absolute percent difference, $MAPD$, is as low as 22–23% in the blue and increases to values slightly above 30% at 555 nm.

For the comparisons of model with data set DS2, the backscattering measurements are available at 490, 510, 532, and 670 nm. This data set is characterized by a large range of backscattering coefficient with $b_{bp}(490)$ values spanning almost three orders of magnitude from 0.002 to 0.86 m^{-1} with a median value of 0.073 m^{-1}. The $b_b(\lambda)$ and $b_{bp}(\lambda)$ coefficients are derived from the model with good accuracy. Owing to consistent dominance of particle backscattering within this data set, the statistical indicators assume similar values for $b_b(\lambda)$ and $b_{bp}(\lambda)$ although $RMSD_{log}$ values are consistently somewhat higher for $b_{bp}(\lambda)$ than $b_b(\lambda)$ (Tables 3 and 4). The MB for both $b_b(\lambda)$ and $b_{bp}(\lambda)$ varies between 0.0035 m^{-1} at 532 nm and 0.015 m^{-1} at 670 nm. The MR values remain within 20% of the value of 1. The $MAPD$ values for both $b_b(\lambda)$ and $b_{bp}(\lambda)$ are about 28–30% in the blue-green spectral region (490 and 555 nm), but increase to 44% at 670 nm. This can be attributed mainly to a slight overestimation of modeled $b_{bp}(670)$ in very turbid waters (i.e., when $b_{bp}(670) > 0.1$ m^{-1}). Because such spectral pattern has not been observed in the analysis with the synthetic data set DS1, this result is likely attributable, at least partly, to larger uncertainties in the in situ measurements of $R_{rs}(670)$ and/or $b_{bp}(670)$ compared with shorter wavelengths for turbid waters. Figure 12 depicts the model-derived versus observed values of $b_{bp}(\lambda)$ for the four wavelengths. The slope of the regression line is close to 1 and the offset parameter is small, which indicates good agreement between the model and measurements over the entire range of observed variability in light backscattering. The regression parameters at 670 nm are, however, noticeably inferior to those at shorter wavelengths, which is consistent with the patterns for the $MAPD$ and $RMSD_{log}$ values in Table 4 (note that similar results apply to $b_b(670)$ in Table 3).

4.5.2. Comparisons for Open Ocean and High Latitude Waters (DS3)

In the data set DS3, $a_{nw}(443)$ ranges from 0.002 to 2.9 m^{-1} and $b_{bp}(550)$ from 0.00029 to 0.053 m^{-1}. The median values of 0.06 m^{-1} for $a_{nw}(443)$ and 0.0013 m^{-1} for $b_{bp}(550)$ are one order of magnitude lower compared with those obtained for DS2, allowing the model to be evaluated over a very different range of bio-optical environments. As no significant differences between different subsets of data within DS3 (e.g., Southern Ocean, Arctic waters, and lower latitude open ocean waters) were observed in terms of model performance, the results are presented for the entire data set DS3.

Table 4
Statistical Indicators for the Performance of the LS2 Model in Retrieving Non-water IOPs at Selected Light Wavelengths, $a_{nw}(\lambda)$ and $b_{bp}(\lambda)$, Based on the Analysis of the DS2, DS3, and DS4 Data Sets

		N^a	r	$RMSD_{log}$	$RMSD$ (m^{-1})	MB (m^{-1})	MR	$MAPD$ (%)
DS2	a_{nw} (412)	170 (0)	0.80	0.158	0.433	0.114	1.118	26.18
	a_{nw} (443)	170 (0)	0.81	0.150	0.322	0.060	1.029	23.09
	a_{nw} (490)	170 (0)	0.78	0.171	0.221	0.003	0.996	23.60
	a_{nw} (510)	166 (0)	0.74	0.190	0.199	−0.008	1.045	27.34
	a_{nw} (555)	146 (0)	0.60	0.248	0.166	−0.015	1.044	33.65
	a_{nw} (670)							
	b_{bp} (412)							
	b_{bp} (443)							
	b_{bp} (490)	188 (0)	0.79	0.183	0.0926	0.0136	1.21	30.84
	b_{bp} (510)	183 (0)	0.83	0.173	0.0767	0.0151	1.11	27.3
	b_{bp} (532)	261 (0)	0.82	0.208	0.0536	0.00354	0.996	28.44
	b_{bp} (670)	252 (6)	0.69	0.294	0.0493	0.0157	1.2	44.03
DS3	a_{nw} (412)	153 (0)	0.93	0.147	0.251	0.0377	0.972	13.33
	a_{nw} (443)	153 (0)	0.92	0.138	0.233	0.0415	0.959	18.51
	a_{nw} (490)	150 (0)	0.86	0.149	0.174	0.032	1.13	20.15
	a_{nw} (510)	128 (22)	0.82	0.28	0.168	0.0258	0.996	23.26
	a_{nw} (555)	145 (2)	0.77	0.317	0.103	0.0177	1.39	45.64
	a_{nw} (670)	46 (111)	0.40	0.553	0.119	0.005	1.03	64.54
	b_{bp} (412)							
	b_{bp} (443)	149 (0)	0.94	0.226	0.0021	0.0004	1.53	52.69
	b_{bp} (490)							
	b_{bp} (510)	145 (0)	0.97	0.178	0.00159	0.0002	1.3	30.47
	b_{bp} (555)	137 (0)	0.96	0.163	0.00164	0.0001	1.26	28.08
	b_{bp} (670)	79 (4)	0.96	0.349	0.001	−0.0002	0.878	29.18
DS4	a_{nw} (412)	105 (0)	0.89	0.164	0.119	−0.0207	0.929	19.33
	a_{nw} (443)	107 (0)	0.89	0.152	0.0888	−0.017	0.925	18.96
	a_{nw} (490)	107 (0)	0.87	0.157	0.0528	−0.00279	1.05	25.57
	a_{nw} (510)	107 (0)	0.86	0.271	0.0423	−0.00424	0.822	33.26
	a_{nw} (555)	102 (4)	0.84	0.379	0.026	0.00585	1.36	64.47
	a_{nw} (670)	51 (48)	0.43	0.694	0.0796	0.0434	3.83	283.2
	b_{bp} (412)	28 (0)	0.35	0.504	0.00226	−0.0004	0.889	32.38
	b_{bp} (443)	28 (0)	0.53	0.166	0.00149	0.00008	0.991	21.89
	b_{bp} (490)	28 (0)	0.70	0.125	0.0011	0.00035	1.13	21.53
	b_{bp} (510)	28 (0)	0.73	0.113	0.000925	0.000128	1.03	18.79
	b_{bp} (555)	28 (0)	0.78	0.125	0.00105	0.000639	1.22	23.2
	b_{bp} (670)	28 (0)	0.66	0.353	0.0014	−0.00019	0.883	36.02

Note. The statistics were calculated in linear space except for $RMSD_{log}$ that was calculated for log-transformed data. [a]The N value indicates the number of stations with both positive in situ and model-derived values, while the value in the parentheses indicates the number of stations with positive in situ measurements but negative model-derived values.

The analysis of DS3 indicates that the total absorption coefficient, $a(\lambda)$, is retrieved with a very good accuracy at all considered wavelengths from 412 to 670 nm (Table 3). For example, the *MR* values remain within 7% around 1 and *MB* varies between about -0.02 m^{-1} at 670 nm and 0.04 m^{-1} at 443 nm. The *MAPD* values range from about 7% in the red to 14% in the blue spectral region.

The comparative analysis of the model and measurements for DS3 supports the notion that the performance of the model for the retrieval of $a_{nw}(\lambda)$ is not as good as for $a(\lambda)$ (Tables 3 and 4). In addition, similar to the results obtained with DS1, the validation of the model with DS3 confirms the finding that $a_{nw}(\lambda)$ can be retrieved with consistently good accuracy only within the short-wavelength (blue) portion of the spectrum (Table 4 and Figure 13). Some deterioration of model performance compared to blue wavelengths is observed at wavelengths as short as 510 nm. In contrast to $a_{nw}(412)$ and $a_{nw}(443)$ where absorption is estimated with good accuracy over the whole range of absorption values, a larger scatter in data around the 1:1 line is observed for $a_{nw}(510)$ values lower than about 0.008 m^{-1} (Figures 13a–13c). This value is about 4 times lower than the absorption coefficient by pure seawater $a_w(510)$. This domain of low absorption values corresponds to very clear waters where absorption by nonwater constituents are much lower than $a_w(\lambda)$. As already discussed in the previous sections, achieving consistently accurate model retrievals of $a_{nw}(\lambda)$ under such conditions is particularly challenging, and this challenge increases as the dominant role of $a_w(\lambda)$ increases with wavelength. This is clearly seen in the analysis conducted with the data set DS3. For example, whereas the $RMSD_{log}$ values for $a_{nw}(\lambda)$ remain below 0.15 in the blue, they increase to 0.28 at 510 nm, 0.32 at 555 nm, and 0.55 at 670 nm (Table 4 and Figure 13d). The *MAPD* values at 555 and 670 nm are significantly higher (about twofold to threefold) than at shorter wavelengths. However, in contrast to $RMSD_{log}$ and *MAPD*, values of *RMSD*, *MB*, and *MR* do not exhibit an increase in the red albeit a significant number of $a_{nw}(670)$ retrievals are negative (Table 4). The *MR* value at 555 nm is 1.39, which is the worst case across the spectrum for this statistical indicator. The spectrally averaged *RMSD* and *MB* values for $a_{nw}(\lambda)$ calculated across the whole spectrum are 0.175 ± 0.06 m^{-1} and 0.027 ± 0.01 m^{-1}, respectively. It is also important to emphasize that in addition to small contribution of a_{nw} to total a in the red spectral region, the challenges for using the LS2 model as well as other inverse reflectance models in this region with input data of $R_{rs}(\lambda)$ determined from in situ measurements are associated with potentially significant uncertainties in the determinations of $R_{rs}(\lambda)$ (e.g., Li et al., 2016).

The model validation with DS3 shows that the total backscattering coefficient, $b_b(\lambda)$, can be retrieved with reasonably good accuracy, although not as good as the retrieval of $a(\lambda)$ (Table 3). For example, for $b_b(\lambda)$ the *MR* values can reach 1.2 and *MAPD* 20%, as opposed to the respective values of 1.08 and 14% for $a(\lambda)$. Although the mean bias *MB* for both $b_b(\lambda)$ and $b_{bp}(\lambda)$ is consistently low, on the order of 10^{-4} m^{-1} regardless of wavelength, other statistical indicators indicate that the model performance is clearly inferior for $b_{bp}(\lambda)$ compared with $b_b(\lambda)$ (Tables 3 and 4). For example, for $b_{bp}(\lambda)$ the range of *MR* is 0.88 – 1.53 and *MAPD* varies between about 28% and 53% (Table 4). The model tends to overestimate $b_{bp}(\lambda)$ in clear waters when $b_{bp}(\lambda)$ values are low, which is particularly well pronounced in the blue-green spectral region for $b_{bp}(\lambda)$ less than about 0.002 m^{-1} (Figure 14). This overestimation corresponds roughly to conditions when

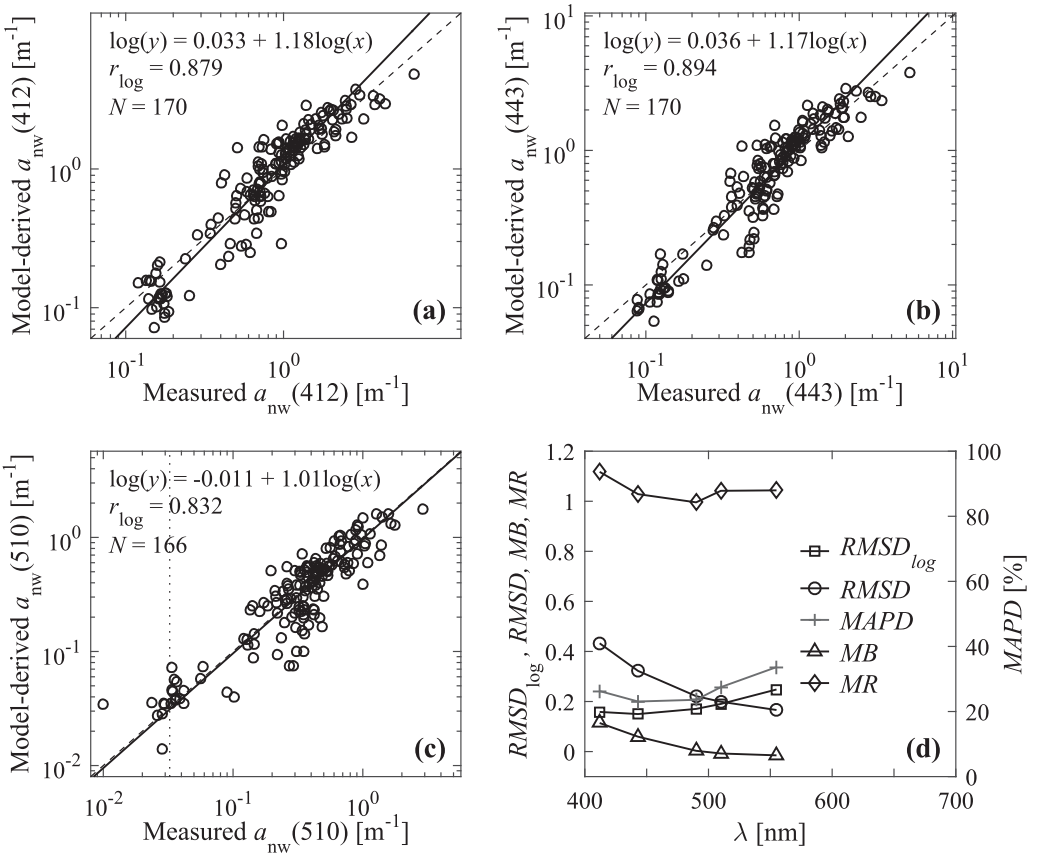

Figure 11. Comparison of model-derived and measured values of nonwater absorption coefficient, a_{nw}, for the data set DS2 for the selected light wavelengths: (a) 412 nm, (b) 443 nm, and (c) 510 nm. The LS2 model was run with input of $R_{rs}(\lambda)$. The $<K_d(\lambda)>_1$ values were derived from the neural network algorithm that has been implemented into the LS2 model using $R_{rs}(\lambda)$ as input. The solid line represents the best fit linear regression type-II fit to log-transformed data and the dashed line represents the 1:1 line. The regression equation (where *x* is the abscissa and *y* the ordinate), values of the Pearson correlation coefficient for log-transformed data r_{log}, and the number of data points *N* are displayed. The vertical line represents the value of pure water absorption coefficient a_w (if not shown, a_w is smaller than the minimum value for the *x* axis scale). (d) Spectra of statistical indicators calculated for the data of model-derived versus measured $a_{nw}(\lambda)$ values (see text for details).

$b_{bp}(\lambda)$ is similar to or lower than the backscattering coefficient of pure seawater, $b_{bw}(\lambda)$. Other inverse reflectance models such as QAA (Lee et al., 2002) and GSM (Maritorena et al., 2002) also exhibit similar challenges in the retrieval of $b_{bp}(\lambda)$ in the oligotrophic waters (Brewin et al., 2012; Huot et al., 2008; Stramski et al., 2008). It is unlikely that this overestimation is related to the formulation of the model because no similar pattern is observed in the model evaluation with the synthetic data set DS1 when the exact values of both $R_{rs}(\lambda)$ and $<K_d(\lambda)>_1$ are used as input parameters (Figure 7b). However, when $R_{rs}(\lambda)$ is used as the sole input parameter to the model, the accuracy of $b_{bp}(\lambda)$ retrieval as examined with DS1 has been shown to slightly decrease in very clear waters (Figure 9b). For such clear waters, a small error in $<K_d(\lambda)>_1$ retrieval has only slight impact on the derivation of $b_b(\lambda)$, but may have a greater effect on $b_{bp}(\lambda)$ depending on the relative proportions of $b_{bw}(\lambda)$ and $b_{bp}(\lambda)$. For example, a comparison of the model-derived and in situ values of $<K_d(\lambda)>_1$ for ultraoligotrophic waters of the South Pacific Gyre sampled during the BIOSOPE cruise shows that $<K_d(\lambda)>_1$ can be estimated with the *MR* of 1.09 and *MAPD* of 10% for $<K_d(\lambda)>_1$ values lower than 0.1 m^{-1} within the blue and green parts of the spectrum. Simple calculations demonstrate that if $<K_d(\lambda)>_1$ is overestimated by 10% in very clear waters, i.e., when $b_{bp}(443) < 0.001$ m^{-1}, the model will overestimate $b_{bp}(443)$ and $b_{bp}(555)$ by 30% and 12%, respectively. Thus, a portion of the discrepancies between the model-derived and in situ measurements of $b_{bp}(\lambda)$, which have been revealed with the model validation for the data set DS3 and presented in Table 4 and Figure 14, appear to be explainable by the uncertainty in $<K_d(\lambda)>_1$ retrieval.

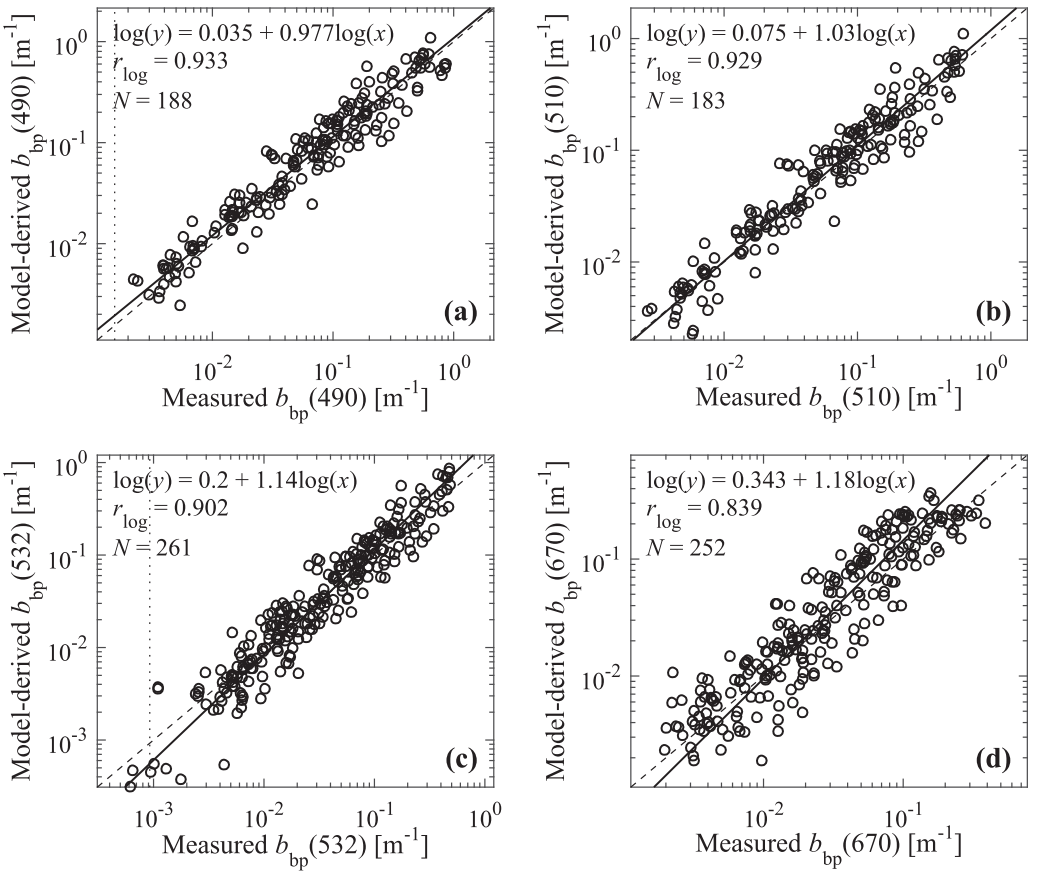

Figure 12. Comparison of model-derived and measured values of the particulate backscattering coefficient, b_{bp}, for the data set DS2 at selected light wavelengths: (a) 490 nm, (b) 510 nm, (c) 532 nm, and (d) 670 nm. The LS2 model was run with input of $R_{rs}(\lambda)$. The $<K_d(\lambda)>_1$ values were derived from the neural network algorithm that has been implemented into the LS2 model using $R_{rs}(\lambda)$ as input. The solid line represents the best fit linear regression type-II fit to log-transformed data and the dashed line represents the 1:1 line. The regression equation (where x is the abscissa and y the ordinate), values of the Pearson correlation coefficient for log-transformed data r_{log}, and the number of data points N are displayed. The vertical line represents the value of pure seawater backscattering coefficient b_{bw} (if not shown, b_{bw} is smaller than the minimum value for the x axis scale).

Other factors can also have an important effect on the accuracy of IOP retrievals, including the retrieval of $b_{bp}(\lambda)$. First, as discussed in section 3.2 the model is sensitive to illumination conditions at the ocean surface, and this sensitivity is more pronounced in very clear waters compared with more turbid waters. Another factor that could partly explain the disagreement between the model-derived and measured $b_{bp}(\lambda)$ in clear waters is related to uncertainties of the in situ measurements. This potential issue has been also addressed by Lee and Huot (2014) to explain the overestimation of $b_{bp}(\lambda)$ by the QAA model in very clear waters, which was observed after the application of correction for Raman scattering to the QAA model (recall that such correction is also applied in our model). Assuming that the $b_{bp}(555)$ measurements can be corrected with an offset value of 0.0002 m^{-1}, Lee and Huot (2014) found a much improved agreement between the QAA-derived and measured $b_{bp}(555)$. By applying a similar correction to our in situ backscattering data from the DS3 data set, we also observe a much improved agreement for $b_{bp}(555)$ (Figure 15). For example, the *MR* decreased from 1.26 (Table 4) to 1.09 (Figure 15) and *MAPD* from 28% (Table 4) to 15.5% (Figure 15). To justify the application of such offset correction, Lee and Huot (2014) indicated that the $b_{bp}(\lambda)$ sensors interrogate a much smaller volume of water than radiometers, and therefore are less sensitive to (or underestimate) the presence of large particles that are relatively scarce. This explanation is, however, difficult to verify quantitatively in our data set, especially as the final values of $b_{bp}(\lambda)$ derived from in situ measurements and representing the near-surface oceanic layer have been typically based on averaging multiple measurements taken at a near-surface depth during a certain

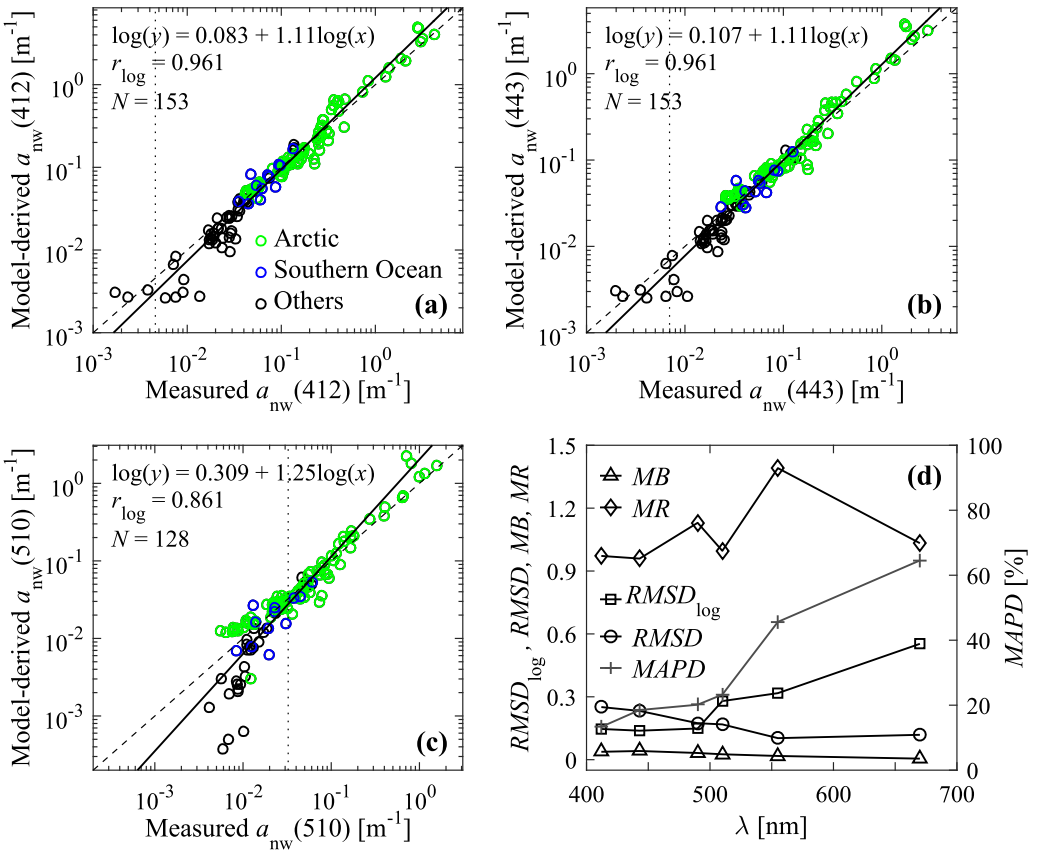

Figure 13. Comparison of model-derived and measured values of nonwater absorption coefficient, a_{nw}, for the data set DS3 at selected light wavelengths: (a) 412 nm, (b) 443 nm, and (c) 510 nm. Field data collected in different regions are indicated by different colors. The LS2 model was run with input of $R_{rs}(\lambda)$. The $<K_d(\lambda)>_1$ values were derived from the neural network algorithm that has been implemented into the LS2 model using $R_{rs}(\lambda)$ as input. The dashed line represents the 1:1 line. The solid line represents the best fit linear regression type-II fit to log-transformed data and the dashed line represents the 1:1 line. The regression equation (where *x* is the abscissa and *y* the ordinate), values of the Pearson correlation coefficient for log-transformed data r_{log}, and the number of data points *N* are displayed. The vertical line represents the value of pure water absorption coefficient a_w. (d) Spectra of statistical indicators calculated for the data of model-derived versus measured $a_{nw}(\lambda)$ values (see text for details).

period of time on the order of minutes and/or binning and averaging multiple measurements taken within a certain range of near-surface depths.

4.6. Model Validation With Satellite and In Situ Match-up Data Set

In the validation analysis based on the satellite and in situ match-up data set (DS4), the satellite-derived $R_{rs}(\lambda)$ is used as the sole input parameter to the LS2 model. The model-derived IOPs are compared with in situ measurements of IOPs that were temporally and spatially matched with the satellite determinations of $R_{rs}(\lambda)$. Similar to the results of the previous section, the statistical indicators calculated on the basis of these match-up comparisons at selected light wavelengths are presented for the total $a(\lambda)$ and $b_b(\lambda)$ in Table 3 and for $a_{nw}(\lambda)$ and $b_{bp}(\lambda)$ in Table 4. Graphical results are shown for $a_{nw}(\lambda)$ and $b_{bp}(\lambda)$ (Figures 16 and 17). This validation analysis accounts for uncertainties related to the estimation of $R_{rs}(\lambda)$ from space observations and other uncertainties inherent to match-up analysis including, for example, in situ measurement uncertainties (including multiple investigators and methodologies) and various issues associated with temporal and/or spatial mismatch between the satellite observations and in situ measurements.

The range of variability of in situ measurements of $a_{nw}(\lambda)$ and $b_{bp}(\lambda)$ in DS4 is similar to that reported in DS3, although DS4 contains less data representative of oligotrophic conditions. The median values of $a_{nw}(443)$ and $b_{bp}(555)$ for DS4 are 0.059 m^{-1} (0.06 m^{-1} for DS3) and 0.0031 m^{-1} (0.0013 m^{-1} for DS3), respectively. The statistical indicators calculated from the match-up data analysis indicate a very good

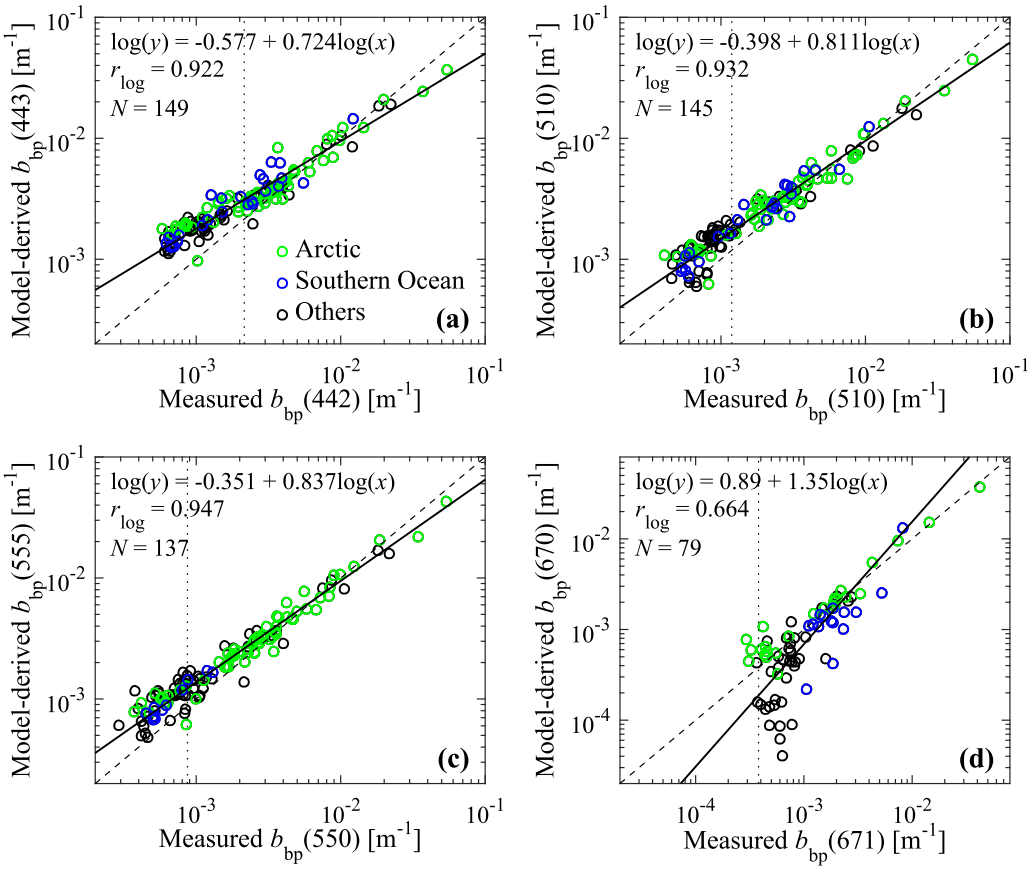

Figure 14. Comparison of model-derived and measured values of the particulate backscattering coefficient, b_{bp}, for the data set DS3 for the selected light wavelengths: (a) 443 nm (442 nm for measured data), (b) 510 nm, (c) 555 nm (550 nm for measured data), and (d) 670 nm (671 nm for measured data). Field data collected in different regions are indicated by different colors. The LS2 model was run with input of $R_{rs}(\lambda)$. The $<K_d(\lambda)>_1$ values were derived from the neural network algorithm that has been implemented into the LS2 model using $R_{rs}(\lambda)$ as input. The solid line represents the best fit linear regression type-II fit to log-transformed data and the dashed line represents the 1:1 line. The regression equation (where x is the abscissa and y the ordinate), values of the Pearson correlation coefficient for log-transformed data r_{log}, and the number of data points N are displayed. The vertical line represents the value of pure seawater backscattering coefficient b_{bw}.

agreement between the model-derived and measured total absorption coefficient, $a(\lambda)$, for all wavelengths considered across the visible spectrum (Table 3). These statistical indicators are comparable to those obtained from the analysis of the data set DS3, and better than those based on the analysis of DS2. These results provide further support of good model performance in terms of retrieving $a(\lambda)$. With regard to the retrieval of nonwater absorption coefficient, $a_{nw}(\lambda)$, the match-up data comparisons demonstrate again that this coefficient can be derived from the model with reasonably good accuracy only within the short-wavelength portion of the spectrum, up to about 510 nm (Table 4 and Figure 16). For example, the *MB*, *MR*, and *MAPD* values for $a_{nw}(443)$ are -0.017 m^{-1}, 0.925, and 19%, respectively. Although these indicators are somewhat inferior to those for $a(443)$, the model performance for $a_{nw}(\lambda)$ in the blue spectral region is good. However, the retrieval accuracy of $a_{nw}(555)$ and $a_{nw}(670)$ deteriorates greatly for the match-up data set DS4. For example, the *MR* values for $a_{nw}(555)$ and $a_{nw}(670)$ are 1.36 and 3.83. In addition, the challenge of retrieving a_{nw} in the red spectral region from satellite-derived $R_{rs}(\lambda)$ is reflected in a significant fraction of model-derived $a_{nw}(670)$ having a negative value (Table 4).

The number of available match-up data points for backscattering is significantly smaller ($N = 28$) compared with the number of data for absorption ($N = \sim 100$). Nevertheless, the analysis of a relatively small match-up data set indicates that the model can assess $b_b(\lambda)$ and $b_{bp}(\lambda)$ with a relatively good accuracy (Tables 3 and 4; Figure 17). The statistical indicators calculated for $b_b(\lambda)$ and $b_{bp}(\lambda)$ based on the data set DS4 are generally

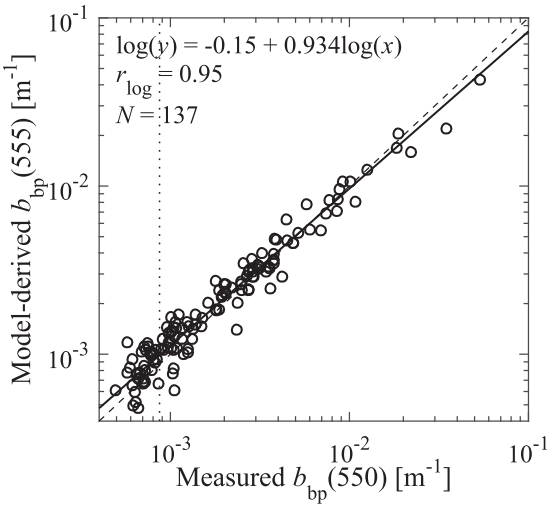

Figure 15. Comparison of model-derived values of the particulate backscattering coefficient, $b_{bp}(555)$, and measured values of $b_{bp}(550)$ for the data set DS3 in which the measured values have been increased by 0.0002 m^{-1} following Lee and Huot (2014). The LS2 model was run with input of $R_{rs}(\lambda)$. The $<K_d(\lambda)>_1$ values were derived from the neural network algorithm that has been implemented into the LS2 model using $R_{rs}(\lambda)$ as input. The solid line represents the best fit linear regression type-II fit to log-transformed data and the dashed line represents the 1:1 line. The regression equation (where *x* is the abscissa and *y* the ordinate), values of the Pearson correlation coefficient for log-transformed data r_{log}, and the number of data points *N* are displayed. The vertical line represents the value of pure seawater backscattering coefficient $b_{bw}(550)$.

similar or better than those calculated for the data sets DS2 and DS3. In addition, although the DS4-based statistical indicators are slightly better for $b_b(\lambda)$ than $b_{bp}(\lambda)$, the latter is still characterized by reasonably good metrics of model performance. For example, the *MB*, *MR*, and *MAPD* values for $b_{bp}(443)$ are 0.00008 m^{-1}, 0.99, and 22%, respectively (Table 4 and Figure 17d). The retrieval accuracy of $b_{bp}(\lambda)$ does, however, decrease noticeably at both ends of the spectrum (412 and 670 nm), where *MR* drops to about 0.89 and *MAPD* is above 30%. This result is similar to the spectral pattern of the relative differences between the satellite-derived $R_{rs}(\lambda)$ and in situ measurements of $R_{rs}(\lambda)$ (Goyens et al., 2013; Jamet et al., 2011).

4.7. Prospects for Model Application to Hyperspectral Data

Whereas the model validation analysis presented above is focused on several discrete spectral bands within the visible part of the spectrum that are consistent with those on heritage and present satellite ocean color sensors (e.g., SeaWiFS, MODIS, MERIS, VIIRS), in recent years significant efforts have been undertaken to develop enhanced capabilities of ocean color remote sensing based on high-spectral resolution measurements. For example, NASA's Plankton, Aerosol, Cloud, ocean Ecosystem (PACE) satellite mission, which is currently in the design phase of development, is intended to provide hyperspectral ocean color observations over a broad spectrum from the ultraviolet (350–400 nm) through visible (400–700 nm) to near-infrared (700–885 nm) at 5 nm intervals, as well as several shortwave infrared bands. This mission will provide an unprecedented capability for observations of the atmosphere and ocean and their roles in Earth's changing climate, including a variety of factors related to marine ecosystems such as the diversity and distribution of phytoplankton communities. As our LS2 model is designed to estimate IOPs from $R_{rs}(\lambda)$ at arbitrary wavelengths, it is of interest to illustrate its prospect for applications in the hyperspectral context.

Figure 18 serves as a preliminary demonstration of model retrievals of $a_{nw}(\lambda)$ and $b_{bp}(\lambda)$ with hyperspectral resolution. For this demonstration three cases of high-spectral resolution in situ measurements of $R_{rs}(\lambda)$ and IOPs were selected from the data set DS3. These cases represent contrasting bio-optical environments. In Figure 18, the model-derived hyperspectral IOPs are compared with the in situ counterparts. Note that in actuality the in situ values of $R_{rs}(\lambda)$ and $a_{nw}(\lambda)$ were obtained from high-spectral resolution measurements (at about 1 nm to a few nanometers intervals), and the $b_{bp}(\lambda)$ values were obtained from measurements at nine spectral bands. For all three cases, the hyperspectral retrievals of $a_{nw}(\lambda)$ compare very well with the measurements over most of the spectral region examined (Figure 18a). The accuracy of model estimates is, however, reduced in the long-wavelength portion of the spectrum including the red spectral region (not shown in Figure 18a), as expected on the basis of our earlier validation analysis (e.g., Figure 13d). For the two environmental cases corresponding to the highest and intermediate values of backscattering, the model-derived magnitude of $b_{bp}(\lambda)$ also compares favorably with the measurements for most wavelengths included in the measurements (Figure 18b). However, for the case with the lowest values of backscattering that corresponds to very clear water, the model retrievals generally overestimate the measurements with the exception of the red spectral region. This result is also consistent with our earlier validation analysis (e.g., Figure 14).

The results in Figure 18 indicate that the model is generally suitable for hyperspectral applications. Importantly, it is expected that this suitability extends to the UV spectral region although the current version of the LS2 model has not been optimized for the UV. In particular, the current $<K_d(\lambda)>_1$ algorithm based on neural network approach has been developed over the limited spectral region from 410 to 670 nm, and it has not been optimized or specifically adapted for accurately estimating $<K_d(\lambda)>_1$ outside this spectral range. In this regard, additional work is required to account for the UV and NIR parts of the spectrum in the learning phase of the neural network. This, in turn, will require collection of in situ measurements of $<K_d(\lambda)>_1$, $R_{rs}(\lambda)$, and IOPs in both UV and NIR. In addition, the current scheme of correction for Raman

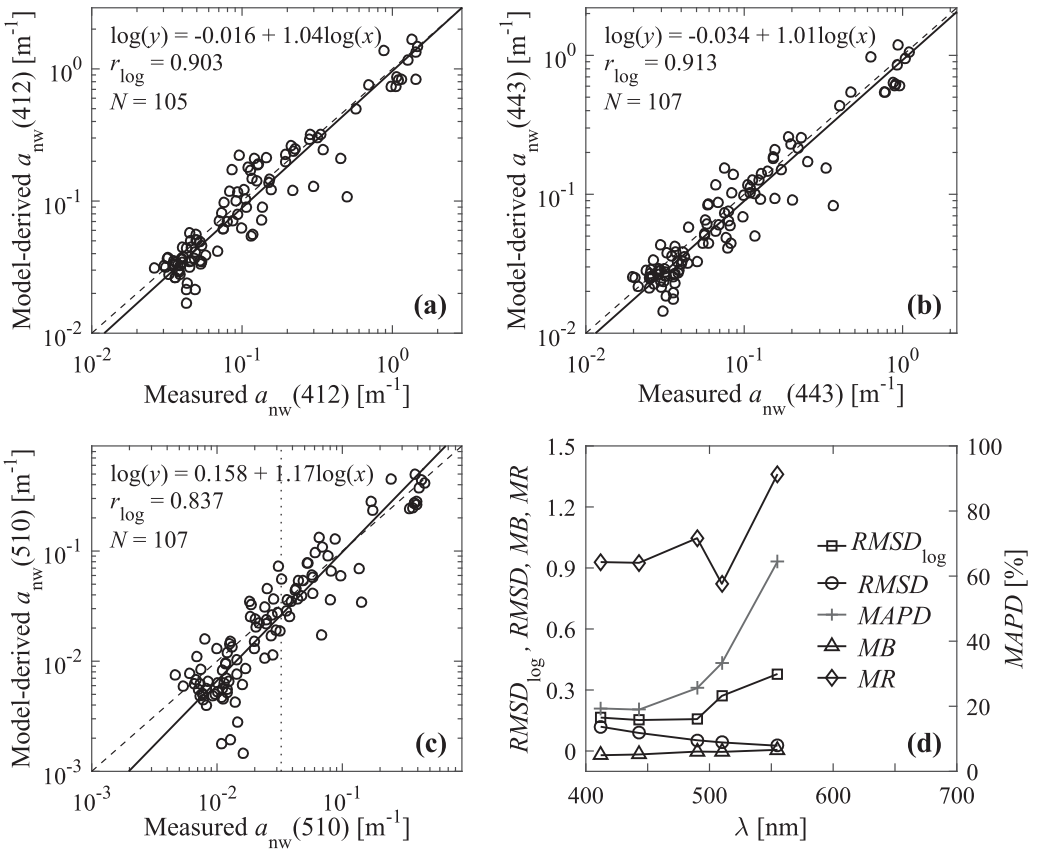

Figure 16. Comparison of model-derived and measured values of the nonwater absorption coefficient, a_{nw}, for the data set DS4 at selected light wavelengths: (a) 412 nm, (b) 443 nm, and (c) 510 nm. The LS2 model was run with input of $R_{rs}(\lambda)$. The $<K_d(\lambda)>_1$ values were derived from the neural network algorithm that has been implemented into the LS2 model using $R_{rs}(\lambda)$ as input. The solid line represents the best fit linear regression type-II fit to log-transformed data and the dashed line represents the 1:1 line. The regression equation (where *x* is the abscissa and *y* the ordinate), values of the Pearson correlation coefficient for log-transformed data r_{log}, and the number of data points *N* are displayed. The vertical line represents the value of pure water absorption coefficient a_w (if not shown, a_w is smaller than the minimum value for the *x* axis scale). (d) Spectra of statistical indicators calculated for the data of model-derived versus measured $a_{nw}(\lambda)$ values (see text for details).

scattering has been developed on the basis of radiative transfer simulations in which the shortest wavelength was 350 nm. Because of the Raman shift in wavelength, this correction is essentially applicable to wavelengths longer than about 400 nm. Although the Raman scattering effect in the UV is not expected to be significant, more rigorous correction within the 350–400 nm spectral region would have to be based on simulations that extend to much shorter UV wavelengths.

5. Conclusions

We modified and improved the original model LS1 (Loisel & Stramski, 2000) for estimating seawater IOPs, specifically the spectral absorption, $a(\lambda)$, and backscattering, $b_b(\lambda)$, coefficients within the ocean surface layer from measurements of ocean reflectance. After subtracting pure seawater contributions, the nonwater absorption, $a_{nw}(\lambda)$, and particulate backscattering, $b_{bp}(\lambda)$, coefficients can also be derived. Similar to the LS1, the modified model, LS2, makes no spectral assumptions about the output IOPs and provides solutions at arbitrary light wavelengths in the visible spectral region independently of one another. This important feature of LS2 alleviates limitations associated with the assumptions about the spectral shape of output IOPs, which are used in most semianalytical inverse reflectance models (e.g., Bukata et al., 1995; Devred et al., 2006; Hoge & Lyon, 1996; Lee et al., 2002; Maritorena et al., 2002; Roesler & Perry, 1995). The LS2 model estimates $a(\lambda)$ and $b_b(\lambda)$ independently of one another, which also avoids drawbacks present in the

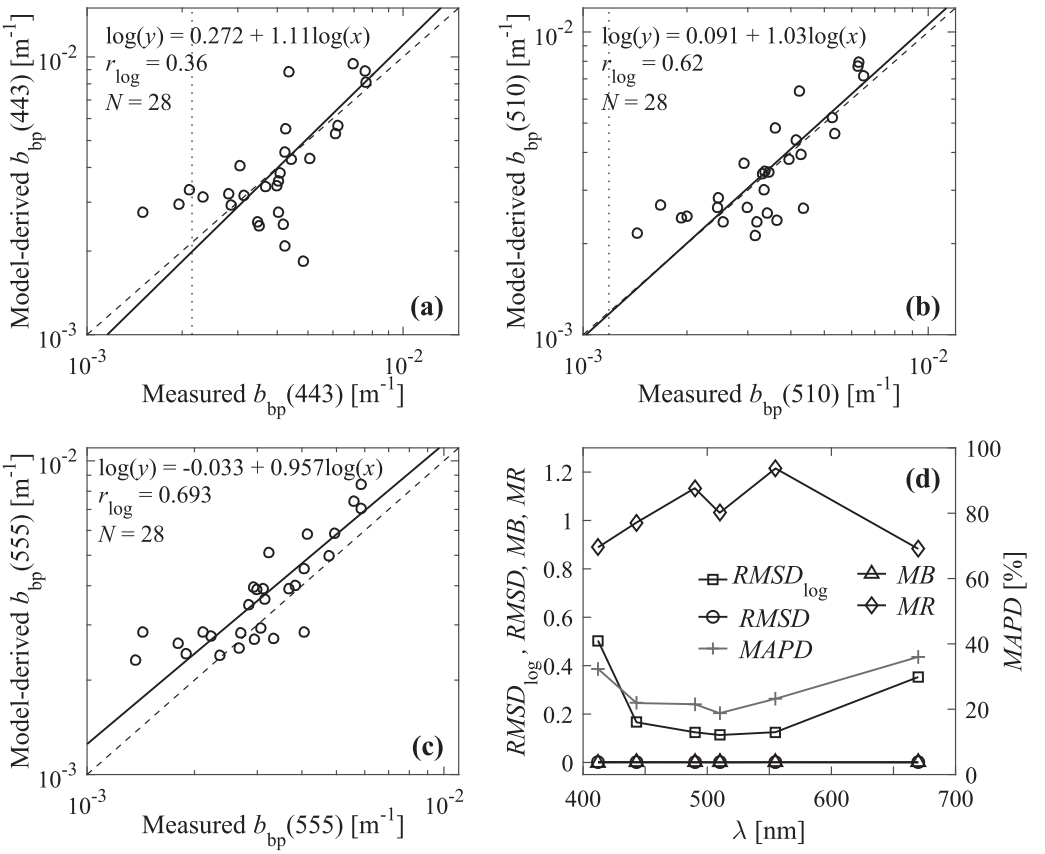

Figure 17. Same as Figure 16 but for the particulate backscattering coefficient, $b_{bp}(\lambda)$. Note, however, the differences in selected light wavelengths in plots (a), (b), and (c) compared with Figure 16.

semianalytical models that use the optimization techniques for simultaneously retrieving IOPs by minimizing differences between the modeled and measured reflectance values. In such optimization schemes the error in one of the retrieved IOPs must be compensated for by errors in other retrieved IOPs. Because the LS2 yields the total IOPs, $a(\lambda)$ and $b_b(\lambda)$, or nonwater IOPs, $a_{nw}(\lambda)$ and $b_{bp}(\lambda)$, it can be applied in combination with stand-alone independently developed models for partitioning the total IOPs into component IOPs

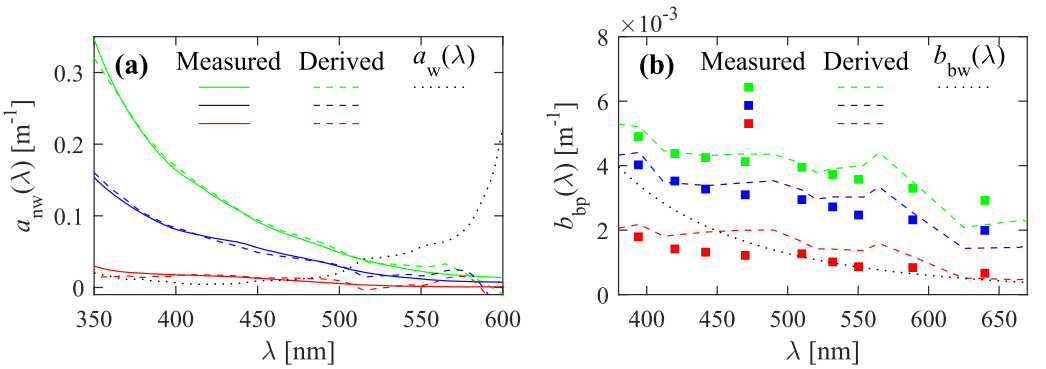

Figure 18. Comparison of high-spectral resolution values derived from the LS2 model with in situ measurements for: (a) nonwater absorption coefficient, $a_{nw}(\lambda)$, and (b) particulate backscattering coefficient, $b_{bp}(\lambda)$. The different colors represent three contrasting cases of measurements extracted from the data set DS3. The spectra of pure water absorption coefficient, $a_w(\lambda)$, and pure seawater backscattering coefficient, $b_{bw}(\lambda)$, are also illustrated. The low, intermediate and high value data for $a_{nw}(\lambda)$ were collected on the BIOSOPE (33°S 81.2°W), ANT26 (41.1°S 53.9°W), and ICESCAPE 2011 (69.9°N 166.2°W) cruises. For $b_{bw}(\lambda)$ all three cases were collected on the ICESCAPE 2011 at the following locations, (73.0°N 160.8°W), (70.9°N 161.7°W), and (69.9°N 166.2°W), respectively.

such as phytoplankton, nonalgal particulate, and CDOM components. For example, the LS2 output of $a_{nw}(\lambda)$ can be used as input to models for partitioning $a_{nw}(\lambda)$ into component absorption coefficients, which do not require reflectance data as input (e.g., Zheng et al., 2015; Zheng & Stramski, 2013). Such combination of LS2 and partitioning models can be useful in applications of remote-sensing observations of ocean color.

When the LS2 is applied in the remote-sensing context, the spectral remote-sensing reflectance, $R_{rs}(\lambda)$, derived, for example, from satellite ocean color measurements, and the solar zenith angle are the required inputs to the model. Note, however, that the LS2 model can be also applied in the context of in situ radiometric measurements providing $R_{rs}(\lambda)$ and the diffuse attenuation coefficient for downwelling irradiance, $<K_d(\lambda)>_1$, as inputs to the model. The latter application scenario generally results in somewhat better performance of the model because of no requirement for estimating $<K_d(\lambda)>_1$ from $R_{rs}(\lambda)$. The structure of LS2 model and its parameterization require the computation of several intermediate parameters. In the context of remote-sensing application, this includes the estimation of $<K_d(\lambda)>_1$ and chlorophyll-*a* concentration, *Chl*, from remotely sensed $R_{rs}(\lambda)$. The $<K_d(\lambda)>_1$ coefficient is obtained from the neural network algorithm using $R_{rs}(\lambda)$ as input. The uncertainty in *Chl* has weak effect on the retrieval of IOPs from LS2 and *Chl* can be derived, for example, from a standard band-ratio reflectance algorithm.

By analyzing a synthetic data set, we determined that when the input of $R_{rs}(\lambda)$ is free of error the performance of the model in retrieving $a(\lambda)$ and $b_b(\lambda)$ is very good across the visible spectral region over a broad range of optical water types. For example, the *MR* values remain generally within 10% around 1 and *MAPD* is about 15% (Figures 8c and 8d). The statistical indicators of model performance for retrieving $a_{nw}(\lambda)$ and $b_{bp}(\lambda)$ deteriorate somewhat but the performance remains satisfactory except for $a_{nw}(\lambda)$ in the long-wavelength (green and red) portion of the spectrum (Figures 9c and 9d). For this spectral region in most oceanic waters that are relatively clear, the total $a(\lambda)$ is dominated greatly by pure water absorption, which makes accurate estimation of $a_{nw}(\lambda)$ extremely difficult and leads to unacceptable performance of the model in a sense that the statistical measures of relative uncertainty become unacceptably large. This difficulty is common in various types of inverse reflectance models.

We also validated the model performance with input of $R_{rs}(\lambda)$ using in situ data sets of radiometric and IOP measurements and comparing the model-derived IOPs with measured IOPs. These data sets cover a broad range of oceanic and coastal environments including many contrasting water bodies such as polar regions, mid-latitude and low-latitude ocean regions, ultraoligotrophic subtropical gyres, and tropical coastal areas affected by large river discharge. Whereas this analysis generally supported good performance of the model in a variety of water bodies, it also clearly demonstrated the limitations of the retrievals of $a_{nw}(\lambda)$ in the long-wavelength part of the spectrum as well as increased uncertainties in the retrievals of $b_{bp}(\lambda)$ in clear ocean waters when $b_{bp}(\lambda)$ is lower than the pure seawater backscattering coefficient $b_{bw}(\lambda)$ (Figures 11–14).

Although the retrievals of nonwater IOPs from inverse reflectance models have rarely been tested in very clear ocean waters, large relative errors in model performance in such waters is naturally expected owing to the very small magnitudes of nonwater IOPs, and their limited contribution to total IOPs renders the inversion scheme highly sensitive to model approximations. Other sources of uncertainties of the LS2 model, which can be more pronounced in very clear waters, include the retrieval of $<K_d(\lambda)>_1$ and the effects of varying illumination conditions at the sea surface associated, for example, with partial cloud cover. Our results also point to the importance of considering potential uncertainties in the IOP measurements when the model is evaluated by comparing model-derived with measured values. In particular, this issue is illustrated for backscattering in very clear waters, where the correction of measured $b_{bp}(555)$ with an offset of 0.0002 m^{-1}, as recommended by Lee and Huot (2014), brings the comparison of model with observations to much better agreement (Figure 15).

Further work is required with special attention devoted to improvements in both the semianalytical inversion schemes and measurement accuracies, especially under circumstances when the models or measurements are subject to significant challenges such as in very clear waters, extremely turbid waters, as well as in the UV, red, and NIR parts of the spectrum. Although the LS2 model shows promise for hyperspectral applications extending beyond the visible spectral range, there is particular need for further testing and extending the spectral range of semianalytical reflectance models to the UV and NIR in view of current

efforts toward future satellite ocean color missions that will cover a broader spectral range with higher spectral resolution compared with the heritage and present missions.

Acknowledgments
This work was supported by Centre National d'Etudes Spatiales in the frame of the COYOTE project (CNES/TOSCA program), and by the NASA Remote Sensing Theory (NNX15AQ53G) and Ocean Biology and Biogeochemistry Programs (NNX15AC55G). Portions of this work were performed during the stay of Hubert Loisel at Scripps Institution of Oceanography during 2017. The in situ measurements gathered in the DS2 data set were mainly collected from different cruises performed in Vietnam coastal waters, French Guyana, and Eastern English Channel through various projects funded by CNES. The data set DS3 is comprised of measurements from two decades of field campaigns supported by NASA, ONR, and NSF. DS1 was created as part of the IOCCG Working Group project on inverse bio-optical algorithms (IOCCG, 2006) and can be found at http://ioccg.org/resources/data/. DS2 and DS3 can be obtained from the World Data Center PANGAEA (https://www.pangaea.de/?t=Oceans). DS4 is derived from version 1.3.sv of the NASA bio-Optical Marine Algorithm Dataset (NOMAD, see Werdell & Bailey, 2005). The authors thank all scientists who participated in or contributed data to these in situ data sets, as well as those who collected and contributed data to the NOMAD data set that was used to create DS4. We thank Jeremy Werdell and an anonymous reviewer for comments on the manuscript.

References

Arnone, R. A., Wood, A. M., & Gould, R. W. (2004). The evolution of optical water mass classification. *Oceanography*, *17*, 14–15.

Balch, W. M., Gordon, H. R., Bowler, B. C., Drapeau, D. T., & Booth, E. S. (2005). Calcium carbonate measurements in the surface global ocean based on Moderate-Resolution Imaging Spectroradiometer data. *Journal of Geophysical Research*, *110*, C07001. https://doi.org/10.1029/2004JC002560

Behrenfeld, M. J., Boss, E., Siegel, D., & Shea, D. M. (2005). Carbon-based ocean productivity and phytoplankton physiology from space. *Global Biogeochemical Cycles*, *19*, GB1006. https://doi.org/1010.1029/2004GB002299

Behrenfeld, M. J., Hu, Y., Hostetler, C. A., Dall'Olmo, G., Rodier, S. D., Hair, J. W., et al. (2013). Space-based lidar measurements of global ocean carbon stocks. *Geophysical Research Letters*, *40*, 4355–4360. https://doi.org/10.1002/grl.50816

Brando, V. E., Dekker, A. G., Park, Y. J., & Schroeder, T. (2012). Adaptive semianalytical inversion of ocean color radiometry in optically complex waters. *Applied Optics*, *51*, 2808–2833.

Brewin, R. J. W., Dall'olmo, G., Sathyendranath, S., & Hardman-Mountford, N. J. (2012). Particle backscattering as a function of chlorophyll and phytoplankton size structure in the open ocean. *Optics Express*, *20*(16), 17632–17652. https://doi.org/10.1364/OE.20.017632

Brewin, R. J. W., Sathyendranath, S., Müller, D., Brockmann, C., Deschamps, P.-Y., Devred, E., et al. (2015). The Ocean Colour Climate Change Initiative: III. A round-robin comparison on in-water bio-optical algorithms. *Remote Sensing of Environment*, *162*, 271–294.

Bricaud, A., Ciotti, A. M., & Gentili, D. (2012). Spatial-temporal variations in phytoplankton size and colored detrital matter absorption at global and regional scales, as derived from twelve years of SeaWiFS data (1998–2009). *Global Biogeochemical Cycles*, *26*, GB1010. https://doi.org/10.1029/2010GB003952

Bukata, R. P., Jerome, J. H., Kondratyev, K. Y., & Pozdnyakov, D. V. (1995). *Optical properties and remote sensing of inland and coastal waters*. Boca Raton, FL: CRC Press.

Campbell, J. W. (1995). The lognormal distribution as a model for bio-optical variability in the sea. *Journal of Geophysical Research*, *100*, 13237–13254.

Chen, J., Quan, W., Cui, T., Song, Q., & Lin, C. (2014). Remote sensing of absorption and scattering coefficient using neural network model: Development, validation, and application. *Remote Sensing of Environment*, *149*, 213–226.

Ciotti, A. M., & Bricaud, A. (2006). Retrievals of a size parameter for phytoplankton and spectral light absorption by Colored Detrital Matter from water-leaving radiances at SeaWiFS channels in a continental shelf region off Brazil. *Limnology and Oceanography Methods*, *4*, 237–253.

Claustre, H., Sciandra, A., & Vaulot, D. (2008). Introduction to the special section Bio-optical and biogeochemical conditions in the South East Pacific in late 2004: The BIOSOPE program. *Biogeosciences*, *5*, 679–691.

Devred, E., Sathyendranath, S., & Platt, T. (2006). Inversion based on semi-analytical reflectance model. In Z. P. Lee (Ed.), *Remote sensing of inherent optical properties: Fundamentals, tests of algorithms and applications, IOCCG Report Series* (Vol. 5, pp. 87–94). Dartmouth, NS: International Ocean-Colour Coordinating Group.

Doerffer, R., & Schiller, H. (2007). The MERIS Case 2 water algorithm. *International Journal of Remote Sensing*, *28*, 517–525.

Doron, M., Babin, M., Mangin, A., & Hembise, O. (2007). Estimation of light penetration, and horizontal and vertical visibility in oceanic and coastal waters from surface reflectance. *Journal of Geophysical Research*, *112*, C06003. https://doi.org/10.1029/2006JC004007

Duforêt-Gaurier, L., Loisel, H., Dessailly, D., Nordkvist, K., & Alvain, S. (2010). Estimates of particulate organic carbon over the euphotic depth from in situ measurements: Application to satellite data over the global ocean. *Deep Sea Research, Part I*, *57*, 351–367.

Dupouy, C., Loisel, H., Neveux, J., Moulin, C., Brown, S., Blanchot, J., et al. (2003). Microbial absorption and backscattering coefficients from in situ and POLDER satellite during an El Nino-Southern Oscillation cold phase in the equatorial Pacific (180°). *Journal of Geophysical Research*, *108*(C12), 8138. https://doi.org/10.1029/2001JC001298

Friedrichs, M. A., Carr, M.-E., Barber, R. T., Scardi, M., Antoine, D., Armstrong, R. A., et al. (2009). Assessing the uncertainties of model estimates of primary productivity in the Tropical Pacific Ocean. *Journal of Marine Systems*, *76*, 113–133. https://doi.org/10.1016/j.jmarsys.2008.05.006

Garver, S. A., & Siegel, D. A. (1997). Inherent optical property inversion of ocean color spectra and its biogeochemical interpretation. 1: Time series from the Sargasso Sea. *Journal of Geophysical Research*, *102*, 18607–18625.

Gordon, H. R. (1993). Sensitivity of radiative transfer to small-angle scattering in the ocean: Quantitative assessment. *Applied Optics*, *32*, 7505–7511.

Gordon, H. R. (1999). Contribution of Raman scattering to water-leaving radiance: A reexamination. *Applied Optics*, *38*, 3166–3174.

Gordon, H. R., Brown, O. B., Evans, R. H., Brown, J. W., Smith, R. C., Baker, K. S., et al. (1988). A semianalytic radiance model of ocean color. *Journal of Geophysical Research*, *93*, 10909–10924.

Gordon, H. R., Brown, O. B., & Jacobs, M. M. (1975). Computed relationships between the inherent and apparent optical properties of a flat homogeneous ocean. *Applied Optics*, *14*, 417–427.

Gordon, H. R., & McCluney, W. R. (1975). Estimation of the depth of sun light penetration in the sea for remote sensing. *Applied Optics*, *14*, 413–416.

Gordon, H. R., & Morel, A. (1983). *Remote assessment of ocean color for interpretation of satellite visible imagery: A review*. New York, NY: Springer.

Goyens, C., Jamet, C., & Schroeder, T. (2013). Evaluation of four atmospheric correction algorithms for MODIS-Aqua images over contrasted coastal waters. *Remote Sensing of Environment*, *131*, 63–75.

Hoge, F. E., & Lyon, P. E. (1996). Satellite retrieval of inherent optical properties by linear matrix inversion of oceanic radiance models: An analysis of model and radiance measurement errors. *Journal of Geophysical Research*, *101*, 16631–16648.

Hu, C., Feng, L., Lee, Z.-P., Davis, C. O., Mannino, A., McClain, C. R., et al. (2012). Dynamic range and sensitivity requirements of satellite ocean color sensors: Learning from the past. *Applied Optics*, *51*, 6045–6062.

Huot, Y., Morel, A., Twardowski, M. S., Stramski, D., & Reynolds, R. A. (2008). Particle optical backscattering along a chlorophyll gradient in the upper layer of the eastern South Pacific Ocean. *Biogeosciences*, *5*, 495–507. https://doi.org/10.5194/bg-5-495-2008

IOCCG (2006). *Remote sensing of inherent optical properties: Fundamentals, tests of algorithms, and applications*. In Z.-P. Lee (Ed.), *Reports of the international ocean-colour coordinating group* (Vol. 5). Dartmouth, NS: International Ocean-Colour Coordinating Group.

Jamet, C., Loisel, H., & Dessailly, D. (2012). Retrieval of the spectral diffuse attenuation coefficient $K_d(\lambda)$ in open and coastal ocean waters using a neural network inversion. *Journal of Geophysical Research: Oceans*, *117*, C10023. https://doi.org/10.1029/2012JC008076

Jamet, C., Loisel, H., Kuchinke, C. P., Ruddick, K., Zibordi, G., & Feng, H. (2011). Comparison of three SeaWiFS atmospheric correction algorithms for turbid waters using AERONET-OC measurements. *Remote Sensing of Environment*, *115*, 1955–1965.
Kostadinov, T. S., Siegel, D. A., & Maritorena, S. (2009). Retrieval of the particle size distribution from satellite ocean color observations. *Journal of Geophysical Research*, *114*, C09015. https://doi.org/10.1029/2009JC005303
Kostadinov, T. S., Siegel, D. A., & Maritorena, S. (2010). Global variability of phytoplankton functional types from space: Assessment via the particle size distribution. *Biogeosciences*, *7*, 3239–3257. https://doi.org/10.5194/bg-7-3239-2010
Lavender, S., Jackson, T., & Sathyendranath, S. (2015). The ocean color climate change initiative: Merging ocean colour seamlessly. *Ocean Challenge*, *21*(1), 29–31.
Laws, E. A. (1997). *Mathematical methods for oceanographers: An introduction*. New York, NY: Wiley-Interscience.
Lee, Z. P., Carder, K. L., & Arnone, R. (2002). Deriving inherent optical properties from water color: A multi-band quasi-analytical algorithm for optically deep waters. *Applied Optics*, *41*, 5755–5772.
Lee, Z. P., Carder, K. L., Steward, R. G., Peacock, T. G., Davis, C. O., & Patch, J. S. (1998). An empirical algorithm for light absorption by ocean water based on color. *Journal of Geophysical Research*, *103*, 27967–27978.
Lee, Z. P., Darecki, M., Carder, K., Davis, C., Stramski, D., & Rhea, W. (2005). Diffuse attenuation coefficient of downwelling irradiance: An evaluation of remote sensing methods. *Journal of Geophysical Research*, *110*, C02017. https://doi.org/10.1029/2004JC002573
Lee, Z. P., & Huot, Y. (2014). On the non-closure of particle backscattering coefficient in oligotrophic oceans. *Optics Express*, *22*(23), 29223–29233. https://doi.org/10.1364/OE.22.029223
Lee, Z. P., Lance, V. P., Shang, S., Vaillancourt, R., Freeman, S., Lubac, B., et al. (2011). An assessment of optical properties and primary production derived from remote sensing in the Southern Ocean (SO GasEx). *Journal of Geophysical Research*, *116*, C00F03. https://doi.org/10.1029/2010JC006747
Legendre, P., & Legendre, L. (1998). Numerical ecology. *Developments in Environmental Modelling*, *20*, 1–853.
Li, L., Stramski, D., & Reynolds, R. A. (2016). Effects of inelastic radiative processes on the determination of water-leaving spectral radiance from extrapolation of underwater near-surface measurements. *Applied Optics*, *55*, 7050–7067.
Loisel, H., Bosc, E., Stramski, D., Oubelker, K., & Deschamps, P.-Y. (2001a). Seasonal variability of the backscattering coefficients in the Mediterranean Sea based on satellite SeaWIFS imagery. *Geophysical Research Letters*, *28*, 4203–4206.
Loisel, H., Lubac, B., Dessailly, D., Duforêt-Gaurier, L., & Vantrepotte, V. (2010). Effect of inherent optical properties variability on the chlorophyll retrieval from ocean color remote sensing: An in situ approach. *Optics Express*, *18*(20), 20949–20959.
Loisel, H., Mériaux, X., Berthon, J. F., & Poteau, A. (2007). Investigation of the optical backscattering to scattering ratio of marine particles in relation to their biogeochemical composition in the eastern English Channel and southern North Sea. *Limnology and Oceanography*, *52*, 739–752.
Loisel, H., Mériaux, X., Poteau, A., Artigas, L. F., Lubac, B., Gardel, A., et al. (2009). Analyze of the inherent optical properties of French Guiana coastal waters for remote sensing applications. *Journal of Coastal Research*, *SI 56*, 1532–1536.
Loisel, H., & Morel, A. (1998). Light scattering and chlorophyll concentration in case 1 waters: A re-examination. *Limnology and Oceanography*, *43*, 847–857.
Loisel, H., Nicolas, J. M., Deschamps, P. Y., & Frouin, R. (2002). Seasonal and inter-annual variability of the particulate matter in the global ocean. *Geophysical Research Letters*, *29*(24), 2196. https://doi.org/10.1029/2002GL015948
Loisel, H., & Poteau, A. (2006). Inversion of IOP based on R_{rs} and remotely retrieved K_d. In Z.-P. Lee (Ed.), *Remote sensing of inherent optical properties: Fundamentals, tests of algorithms and applications, IOCCG Report* (Vol. 5, pp. 35–41). Dartmouth, NS: International Ocean-Colour Coordinating Group.
Loisel, H., & Stramski, D. (2000). Estimation of the inherent optical properties of natural waters from the irradiance attenuation coefficient and reflectance in the presence of Raman scattering. *Applied Optics*, *39*, 3001–3011.
Loisel, H., Stramski, D., Mitchell, B. G., Fell, F., Fournier-Sicre, V., Lemasle, B., et al. (2001b). Comparison of the ocean inherent optical properties obtained from measurements and inverse modeling. *Applied Optics*, *40*, 2384–2397.
Loisel, H., Vantrepotte, V., Ouillon, S., Ngoc, D. D., Herrmann, M., Tran, V., et al. (2017). Assessment and analysis of the chlorophyll-a concentration variability over the Vietnamese coastal waters from the MERIS ocean color sensor (2002–2012). *Remote Sensing of Environment*, *190*, 217–232. https://doi.org/10.1016/j.rse.2016.12.016
Loisel, H., Vantrepotte, V., Norkvist, K., Mériaux, X., Kheireddine, M., Ras, J., et al. (2011). Characterization of the bio-optical anomaly and diurnal variability of particulate matter, as seen from scattering and backscattering coefficients, in ultra-oligotrophic eddies of the Mediterranean Sea. *Biogeosciences*, *8*, 3295–3317. https://doi.org/10.5194/bg-8-3295-2011
Lubac, B., Loisel, H., Guiselin, N., Astoreca, R., Artigas, L. F., & Mériaux, X. (2008). Hyperspectral versus multispectral remote sensing approach to detect phytoplankton blooms in coastal waters: Application to a *Phaeocystis globosa* bloom. *Journal of Geophysical Research*, *113*, C06026. https://doi.org/10.1029/2007JC004451
Mannino, A., Russ, M., & Hooker, S. (2008). Algorithm development and validation for satellite-derived distributions of DOC and CDOM in the US Middle Atlantic Bight. *Journal of Geophysical Research*, *113*, C07051. https://doi.org/10.1029/2007JC004493
Maritorena, S., Siegel, D. A., & Peterson, A. (2002). Optimization of a semi-analytic ocean color model for global scale applications. *Applied Optics*, *41*, 2705–2714.
Marshall, B. R., & Smith, R. C. (1990). Raman scattering and in-water optical properties. *Applied Optics*, *29*, 71–84.
Melin, F., Zibordi, G., & Berthon, J.-F. (2007). Assessment of satellite ocean color products at a coastal site. *Remote Sensing of Environment*, *110*, 192−−215.
Mitchell, B. G., Kahru, M., Wieland, J., & Stramska, M. (2003). Determination of spectral absorption coefficients of particles, dissolved material and phytoplankton for discrete water samples. In J. L. Mueller, G. S. Fargion, & C. R. McClain (Eds.), *Ocean optics protocols for satellite ocean color sensor validation* (NASA/TM-2003–211621, pp. 39–64). Greenbelt, MD: NASA Goddard Space Flight Center.
Mobley, C. D. (1994). *Light and water: Radiative transfer in natural waters*. New York, NY: Academic Press.
Mobley, C. D., & Sundman, L. K. (2008). *Hydrolight 5-Ecolight 5 technical documentation*. Bellevue, WA: Sequoia Scientific, Inc.
Morel, A., & Loisel, H. (1998). Apparent optical properties of oceanic water: Dependence on the molecular scattering contribution. *Applied Optics*, *37*, 4765–4776.
Morel, A., & Maritorena, S. (2001). Bio-optical properties of oceanic waters: A reappraisal. *Journal of Geophysical Research*, *106*, 7163–7180.
Morel, A., & Prieur, L. (1977). Analysis of variations in ocean color. *Limnology and Oceanography*, *22*, 709–722.
Neukermans, G., Loisel, H., Meriaux, X., Astoreca, R., & McKee, D. (2012). In situ variability of mass-specific beam attenuation and backscattering of marine particles with respect to particle size, density, and composition. *Limnology and Oceanography*, *57*, 124–144.
Neukermans, G., Reynolds, R. A., & Stramski, D. (2016). Optical classification and characterization of marine particle assemblages within the western Arctic Ocean. *Limnology and Oceanography*, *61*, 1472–1494. https://doi.org/10.1002/lno.10316

O'Reilly, J. E., Maritorena, S., Mitchell, B. G., Siegel, D. A., Carder, K. L., Garver, S. A., et al. (1998). Ocean color chlorophyll algorithms for SeaWiFS. *Journal of Geophysical Research*, *103*, 24937–24953.

O'Reilly, J. E., Maritorena, S., Siegel, D. A., O'Brien, M. C., Toole, D., Mitchell, B. G., et al. (2000). In S. B. Hooker & E. R. Firestone (Eds.), *SeaWiFS post-launch calibration and validation analyses, Part 3* (NASA/TM-2000–206892, Vol. 11, 49 p.). Greenbelt, MD: NASA Goddard Space Flight Center.

Pan, X., Mannino, A., Russ, M. E., & Hooker, S. B. (2008). Remote sensing of the absorption coefficient and chlorophyll a concentration in the United States southern Middle Atlantic Bight from SeaWiFS and MODIS-Aqua. *Journal of Geophysical Research*, *113*, C11022. https://doi.org/10.1029/2008JC004852

Petzold, T. J. (1972). *Volume scattering functions for selected natural waters* (Scripps Inst. Oceanogr. Contrib. 72–78). San Diego, CA: Scripps Institution of Oceanography.

Pinkerton, M. H., Moore, G. F., Lavender, S. J., Gall, M. P., Oubelkheir, K., Richardson, K. M., et al. (2006). A method for estimating inherent optical properties of New Zealand continental shelf waters from satellite ocean colour measurements. *New Zealand Journal of Marine and Freshwater Research*, *40*, 227–247.

Reynolds, R. A., Stramski, D., & Mitchell, B. G. (2001). A chlorophyll-dependent semianalytical reflectance model derived from field measurements of absorption and backscattering coefficients within the Southern Ocean. *Journal of Geophysical Research*, *106*, 7125–7138. https://doi.org/10.1029/1999JC000311

Reynolds, R. A., Stramski, D., & Neukermans, G. (2016). Optical backscattering of particles in Arctic seawater and relationships to particle mass concentration, size distribution, and bulk composition. *Limnology and Oceanography*, *61*, 1869–1890. https://doi.org/10.1002/lno.10341

Roesler, C. S., & Perry, M. J. (1995). In situ phytoplankton absorption, fluorescence emission, and particulate backscattering spectra determined from reflectance. *Journal of Geophysical Research*, *100*, 13279–13294.

Siegel, D. A., Maritorena, S., Nelson, N. B., Hansell, D. A., & Lorenzi-Kaiser, M. (2002). Global distribution and dynamics of colored dissolved and detrital organic materials. *Journal of Geophysical Research*, *107*(C12), 3228. https://doi.org/10,1029/2001JC000965

Smyth, T. J., Moore, G. F., Hirata, T., & Aiken, J. (2006). Semianalytical model for the derivation of ocean color inherent optical properties: Description, implementation, and performance assessment. *Applied Optics*, *45*, 8116–8131.

Stavn, R. H. (1993). Effects of Raman scattering across the visible spectrum in clear ocean water: A Monte Carlo study. *Applied Optics*, *32*, 6853–6863.

Stow, C. A., Jolliff, J., McGillicuddy, D. J., Doney, S. C., Allen, J. I., Friedrichs, M. A. M., et al. (2009). Skill assessment for coupled biological/physical models of marine systems. *Journal of Marine Systems*, *76*, 4–15. https://doi.org/10.1016/j.jmarsys.2008.03.011

Stramska, M., Stramski, D., Hapter, R., Kaczmarek, S., & Stoń, J. (2003). Bio-optical relationships and ocean color algorithms for the north polar region of the Atlantic. *Journal of Geophysical Research*, *108*(C5), 3143. https://doi.org/10.1029/2001JC001195

Stramski, D., Reynolds, R. A., Babin, M., Kaczmarek, S., Lewis, M. R., Röttgers, R., et al. (2008). Relationships between the surface concentration of particulate organic carbon and optical properties in the eastern South Pacific and eastern Atlantic Oceans. *Biogeosciences*, *5*, 171–201. https://doi.org/10.5194/bg-5-171-2008

Stramski, D., Reynolds, R. A., Kaczmarek, S., Uitz, J., & Zheng, G. (2015). Correction of pathlength amplification in the filter-pad technique for measurements of particulate absorption coefficient in the visible spectral region. *Applied Optics*, *54*, 6763–6782.

Stramski, D., Reynolds, R. A., Kahru, M., & Mitchell, B. G. (1999). Estimation of particulate organic carbon in the ocean from satellite remote sensing. *Science*, *285*, 239–241.

Sugihara, S., Kishino, M., & Okami, M. (1984). Contribution of Raman scattering to upward irradiance in the sea. *Journal of the Oceanographical Society of Japan*, *40*, 397–404.

Traykovski, L. V. M., & Sosik, H. M. (2003). Feature-based classification of optical water types in the Northwest Atlantic based on satellite ocean color data. *Journal of Geophysical Research*, *108*(C5), 3150. https://doi.org/10.1029/2001JC001172

Uitz, J., Stramski, D., Reynolds, R. A., & Dubranna, J. (2015). Assessing phytoplankton community composition from hyperspectral measurements of phytoplankton absorption coefficient and remote-sensing reflectance in open-ocean environments. *Remote Sensing of Environment*, *171*, 58–74. https://doi.org/10.1016/j.rse.2015.09.027

Vantrepotte, V., Loisel, H., Mélin, F., Dessailly, D., & Duforêt-Gaurier, L. (2011). Global particulate matter pool temporal variability over the SeaWiFS period (1997–2007). *Geophysical Research Letters*, *38*, L02605. https://doi.org/10.1029/2010GL046167

Wang, P., Boss, E. S. & Roesler, (2005). Uncertainties of inherent optical properties obtained from semianalytical inversions of ocean color. *Applied Optics*, *44*, 4074–4085.

Wang, M., Son, S., & Harding, L. W. Jr. (2009). Retrieval of diffuse attenuation coefficient in the Chesapeake Bay and turbid ocean regions for satellite ocean color applications. *Journal of Geophysical Research*, *114*, C10011. https://doi.org/10.1029/2009JC005286

Werdell, P. J., & Bailey, S. W. (2005). An improved in situ bio-optical data set for ocean color algorithm development and satellite data product validation. *Remote Sensing of Environment*, *98*, 122–140.

Werdell, P. J., Franz, B. A., Bailey, S. W., Feldman, G. W., Boss, E., Brando, V. E., et al. (2013). Generalized ocean color inversion model for retrieving marine inherent optical properties. *Applied Optics*, *52*, 2019–2037.

Westberry, T. K., Boss, E., & Lee, Z.-P. (2013). Influence of Raman scattering on ocean color inversion models. *Applied Optics*, *52*, 5552–5561.

Yang, H., Arnone, R., & Jolliff, J. (2015). Estimating advective near-surface currents from ocean color satellite images. *Remote Sensing of Environment*, *158*, 1–14. https://doi.org/10.1016/j.rse.2014.11.010

Zhang, T., & Fell, F. (2007). An empirical algorithm for determining the diffuse attenuation coefficient Kd in clear and turbid waters from spectral remote sensing reflectance. *Limnology and Oceanography Methods*, *5*, 457–462.

Zhang, X., Huot, Y., Bricaud, A., & Sosik, H. M. (2015). Inversion of spectral absorption coefficients to infer phytoplankton size classes, chlorophyll concentration, and detrital matter. *Applied Optics*, *54*, 5905–5816.

Zheng, G., & Stramski, D. (2013). A model based on stacked-constraints approach for partitioning the light absorption coefficient of seawater into phytoplankton and non-phytoplankton components. *Journal of Geophysical Research: Oceans*, *118*, 2155–2174. https://doi.org/10.1002/jgrc.20115

Zheng, G., Stramski, D., D., & DiGiacomo, P. M. (2015). A model for partitioning the light absorption coefficient of natural waters into phytoplankton, nonalgal particulate, and colored dissolved organic components: A case study for the Chesapeake Bay. *Journal of Geophysical Research: Oceans*, *120*, 2601–2621. https://doi.org/10.1002/2014JC010604

Zheng, G., Stramski, D., & Reynolds, R. A. (2014). Evaluation of the Quasi-Analytical Algorithm for estimating the inherent optical properties of seawater from ocean color: Comparison of Arctic and lower-latitude waters. *Remote Sensing of Environment*, *155*, 194–209.

Zibordi, G., Melin, F., & Berthon, J. F. (2006). Comparison of SeaWiFS, MODIS and MERIS radiometric products at a coastal site. *Geophysical Research Letters*, *33*, L06617. https://doi.org/10.1029/2006GL025778